



Contents lists available at ScienceDirect

Journal of Sound and Vibration

journal homepage: www.elsevier.com/locate/jsvi

3-D thermoacoustic instability analysis based on Green's function approach

Xiaoyu Wang^a, Maria Heckl^{b,*}

^a Research Institute of Aero-Engine, Beihang University, Beijing, 100191, China

^b School of Chemical and Physical Sciences, Keele University, Staffordshire ST5 5BG, UK

ARTICLE INFO

Keywords:

Green's function
furnace
mode interference
thermoacoustic instability

ABSTRACT

A fundamental analysis is made of the thermoacoustic instability in a hard-walled box. We model the flame as an acoustically compact source with a heat release characteristic described by a directional $n\tau$ -law. This has the following features: it gives the heat release rate in terms of the acoustic velocity at an earlier time τ ; it is linear with coupling coefficient n ; the "flame surface" is a small flat patch with variable orientation.

We derive an integral equation for the acoustic field by using a Green's function tailored to a 3-D rectangular box with hard-wall boundary conditions. The integral equation is solved by two methods. Firstly, an iteration method, stepping forward in time, is used to give the time history of the acoustic velocity. By analysing this time history, we investigate the interference between two (or more) thermoacoustic modes. In the second method, we apply a Laplace transform to determine the thermoacoustic eigenfrequency and growth rate of thermoacoustic modes. This method is suitable for parameter studies, and we use it to investigate the effect of the flame orientation and flame position on the thermoacoustic instability. We show results for the 2-D case. They reveal that the stability behaviour depends strongly on the flame orientation and on the flame position in the xy -plane. We also show results for the interference between different thermoacoustic modes, especially for cases where there are two acoustic modes with similar frequencies.

1. Introduction

Instabilities caused by a thermoacoustic feedback mechanism are observed in various combustion systems, such as gas turbines, rocket engines, and furnaces. When they occur, they cause excessive noise, potentially resulting in structural damage; they can also exacerbate pollution by combustion products. There are many factors that affect thermoacoustic instabilities, some of which are well understood, while others are the subject of ongoing research. One can get an overview in the review articles [1–3], in the books [4,5], and in [6].

The studies can be divided loosely into one-, two- and three-dimensional studies, where the "dimension" applies to the number of spatial dimensions that the acoustic waves can vary in.

One-dimensional studies tend to be made for combustion chambers whose length is considerably larger than the dimension characterising their cross-section. Many laboratory test rigs have this feature, and when they are modelled theoretically, this is typically done with a network model. Early examples, involving longitudinal waves travelling parallel to the burner axis are:

* Corresponding author.

E-mail address: m.a.heckl@keele.ac.uk (M. Heckl).

<https://doi.org/10.1016/j.jsv.2022.116816>

Received 20 May 2021; Received in revised form 30 January 2022; Accepted 1 February 2022

Available online 3 February 2022

0022-460X/© 2022 The Authors. Published by Elsevier Ltd. This is an open access article under the CC BY-NC-ND license (<http://creativecommons.org/licenses/by-nc-nd/4.0/>).

List of symbols

c	speed of sound
f_p	pressure distribution in standing wave field in cavity
f_u	velocity distribution in standing wave field in cavity
$f_{pu} = -f_p f_u$	product of pressure and velocity distribution in cavity
$f(t)$	forcing term in integral equation
G	Green's function
$G_{mnk} = \frac{\partial g_{mnk}}{\partial r} \Big _{\vec{r}=\vec{r}_q}$	gradient of the Green's function amplitude at the flame position
$g_{mnk}(\vec{r}, \vec{r}')$	amplitude of mode (m, n, k) in the Green's function
H_x, H_y, H_z	side lengths of rectangular cavity
h	small time step
j	imaginary unit
$K(t, t')$	integral kernel
$K_q = \overline{Q}/(\bar{u}_r \bar{\rho})$	measure for mean heat release rate (constant)
k_x, k_y, k_z	allowed wave numbers of cavity modes
$k_0 = \omega/c$	wave number
$k_{mnk} = \sqrt{k_x^2 + k_y^2 + k_z^2}$	magnitude of allowed wave number vector in cavity
L	length of 1-D cavity
M	integer to discretise time-lag τ
m, n, k	mode numbers of acoustic modes in cavity
N	integer to discretise time t
n	coupling coefficient in the heat release law
Q	global heat release rate
q	local heat release rate (per unit mass)
R_0, R_L	reflection coefficients
RI	Rayleigh index
$\vec{r} = (x, y, z)$	observer position
$\vec{r}' = (x', y', z')$	source position
\vec{r}_q	position of flame
t	time
$u'_q(t) = u'_r(\vec{r}_q, t)$	value of u'_r at the flame position \vec{r}_q
$u'_r(\vec{r}, t)$	velocity component normal to the flame surface
$u_{\mu\nu\kappa}$	complex velocity amplitude of thermoacoustic modes in cavity
x_q	x-coordinate of flame position
y_q	y-coordinate of flame position
Γ_{mnk}	volume integral of products of eigenfunctions
γ	specific heat ratio
δ	delta function
ε	small angle
$\varepsilon_m, \varepsilon_n, \varepsilon_k$	constants that take values 1 or 2
θ	angle between flame surface normal and z-axis
μ, ν, κ	mode numbers of thermoacoustic cavity modes
$\bar{\rho}$	mass density in cavity
τ	time-lag
ϕ	velocity potential
ϕ_0	initial value of ϕ at the flame position
φ	angle between flame surface normal and x-axis
Ψ_{mnk}	cavity eigenfunction
$\Omega_{\mu\nu\kappa}$	thermoacoustic eigenfrequency in cavity (complex)
ω	angular frequency
ω_{mnk}	frequency of mode (m, n, k) in the Green's function, i.e. allowed frequencies of cavity modes

Overbars denote the mean part of field quantities, primes denote the fluctuating part of field quantities in the time-domain, and hats denote the fluctuating part of field quantities in the frequency-domain. For example, for the heat release rate, the mean part is \bar{Q} , and the fluctuating part is Q' in the time-domain and \hat{Q} in the frequency-domain.

The time dependence of a quantity oscillating with frequency ω is denoted by $e^{j\omega t}$

- the premixed laminar burner [7] and the multiple-inlet combustor [8] investigated by Candel's group,
- the reheat-buzz rig studied by Dowling's group [9],
- the electrically heated Rijke tube developed by Heckl [10,11].

More recent examples tend to focus on nonlinear aspects, such as:

- the multiple-injection burner investigated in [12].
- the horizontal Rijke tube studied by Sujith's group [13,14]
- the turbulent bluff-body burner studied in [15]
- the study in [16], where a network model was developed for a long flame by segmenting the flame axially and connecting the segments with jump conditions.

Also falling into the one-dimensional category are azimuthal waves in combustion systems with *annular* geometry. The papers [17–20] have proposed network models to analyse 1-D azimuthal thermoacoustic modes.

Combustion systems, where the acoustic field can vary in *two* dimensions, include annular combustors and rectangular combustors. In annular combustion systems, this typically involves variations in the *axial and azimuthal* directions. Analytical studies in this area have been made in [21,22] (amongst others), proposing network models for the combined effect of axial and azimuthal velocity perturbations, and predict the complex frequencies and mode shapes of individual modes, not just the unstable ones. More recently, Li and Sun [23] studied mixed axial-azimuthal modes in the presence of vorticity waves with a network model.

Most thermoacoustic simulations are done by mesh-based numerical approaches, which vary in terms of accuracy and computational cost. One such approach is based on the nonhomogeneous Helmholtz equation and commonly called "Helmholtz solver" [24]. The Helmholtz equation is discretised in physical space by a finite-element method, then combined with a heat release law, and converted into an eigenvalue problem involving a large (but finite) matrix. The eigenvalues of this matrix give the complex eigenfrequencies, and the corresponding eigenvectors give the mode shapes. This method is suitable for configurations where the acoustics is linear, the mean flow is negligible, and the mean pressure is uniform; the speed of sound may have spatial variations. Helmholtz solvers predict the frequencies and growth rates, as well as the mode shapes of *all* possible modes, not just the unstable ones. This capability, together with their modest computational cost, makes them a popular choice for thermoacoustic simulations. Compared with network models, they are more versatile in terms of combustor geometry, but require more computational effort.

The Helmholtz solver has been applied to laboratory test rigs as well as industrial burners. An application to the swirl test rig described in [25] can be found in [26]. The MICCA test rig (an annular combustion rig with multiple matrix burners, see [27]), exhibits combustion instabilities involving two modes (a standing azimuthal mode and an axial mode) with coinciding frequencies; this was modelled with a Helmholtz solver in [28]. Both studies assumed a weakly nonlinear heat release law and predicted not only the frequencies and mode shapes, but also the limit cycle amplitudes. An example of a Helmholtz solver applied to an *industrial* gas turbine can be found in [29].

In contrast to network models and Helmholtz solvers, methods based on computational fluid dynamics (CFD) do not give information on individual modes, but on the spatio-temporal evolution of the mean and fluctuating field quantities. They are available with different levels of accuracy and computational cost. In order of increasing cost, they are: the unsteady Reynolds-averaged Navier–Stokes (URANS) method, large eddy simulation (LES), and direct numerical simulation (DNS). They give precise results for the effect of complex geometries, complex flow patterns and multiple sources. Examples of applications to rectangular geometries can be found in [30–32]; cylindrical or annular geometries have been modelled in [33,34].

Analytical modelling is the method of choice, if physical insight is a priority. The most commonly used analytical tools are network models. For rectangular geometries, these have been 1-D, and they have even been applied to furnaces, where the acoustic field is clearly 3-D [35,36]. As far as we know, there are no fundamental investigations of thermoacoustic effects in the kind of rectangular cavity shown in Fig. 1. This is the gap that the present paper is trying to fill, i.e. our aim is to enhance the physical understanding of the 2-D and 3-D cases.

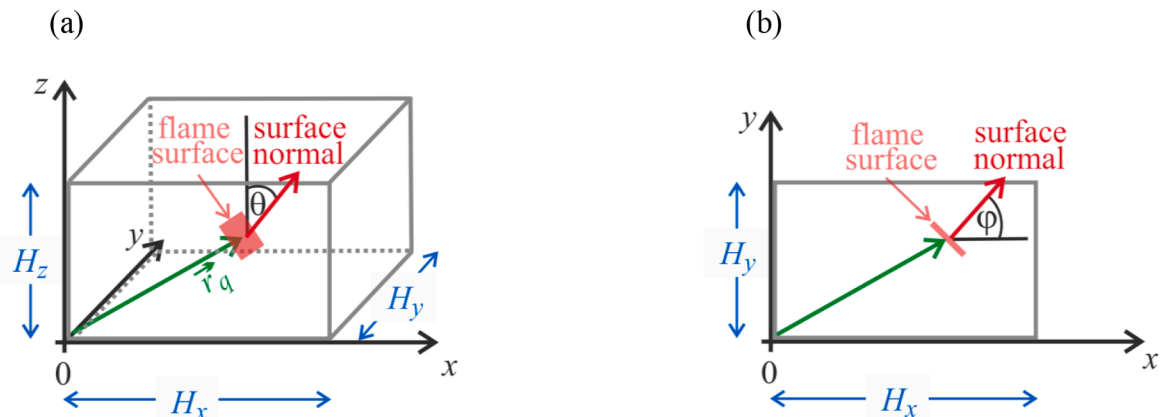


Fig. 1. Schematic of the rectangular combustion chamber; (a) 3-D geometry, (b) geometry for case of no z -dependence. The flame surface is a small flat patch with a surface normal whose orientation is described by the angles θ and φ .

Our approach is based on the tailored Green’s function (the acoustic field that is generated by an impulsive point source in a cavity). It is an extension of the work by Heckl and Howe [37,38], who pioneered the use of the tailored Green’s function to model 1-D thermoacoustic systems. By extending this approach to 3-D, we will be able to determine the acoustic field generated by thermoacoustic feedback involving a compact flame in a box. We will gain new insight into effects not found in 1-D cavities, such as interference of the many modes that are present in a 3-D cavity, and the effect of the flame orientation.

This paper is structured as follows. Section 2 introduces the tailored Green’s function for the 3-D situation, the model of the compact flame and the governing equation for the normal acoustic velocity in terms of the Green’s function. Validation of our model and code is shown in Section 3. In Section 4 we investigate the influence of flame angle and flame position for a single-frequency resonator. Section 5 gives the results for the interference effects between co-existing modes. Conclusions are drawn in Section 6.

2. The integral governing equation and solution

We present our Green’s function approach in three steps. In the first step (Section 2.1), we explain the concept of the tailored Green’s function, which describes the acoustic field in the cavity *without* a flame. In the second step (Section 2.2), we introduce the flame model, which describes how the rate of heat released by the flame depends on the local acoustic field. These two elements of our model are combined in the third step (Section 2.3), where we derive an integral equation for the acoustic field in the cavity *with* flame. This integral equation captures the two-way coupling between the acoustic field and the fluctuating heat release rate.

2.1. The 3-D tailored Green’s function

As this is a fundamental study, we consider an idealised configuration with the geometry shown in Fig. 1. The combustion chamber is modelled as a hard-walled cavity with side lengths H_x , H_y and H_z . We assume that the Mach number of any mean flow is low enough to satisfy $M^2 \ll 1$. There is then no need to account for the frequency drop caused by the phenomenon that sound waves travelling in the direction of the flow have a higher speed than those travelling against the flow (see [39], page 698). In a further idealisation, we assume that the mean temperature in the cavity is uniform. This is obviously not the case in a real combustion chamber, where the mean temperature across the flame can jump by many hundreds of Kelvin, depending on the power of the flame. Finally, we exclude entropy waves. Our assumptions may seem unrealistic, however, our study is fundamental, and we focus on the effects of the following features:

- the acoustic field varies not just in 1-D, but in 2-D or 3-D
- the orientation of the flame can change relative to the acoustic field.

The Green’s function tailored to the hard-walled cavity shown in Fig. 1, i.e. the response at an observer point $\vec{r} = (x, y, z)$ in the box due to an impulsive point source at $\vec{r}' = (x', y', z')$ in the box, is denoted by $G(\vec{r}, \vec{r}', t - t')$; $t - t'$ is the time it takes the signal to travel from \vec{r}' to \vec{r} . The governing equation is the non-homogeneous wave equation,

$$\frac{1}{c^2} \frac{\partial^2 G}{\partial t^2} - \nabla^2 G = \delta(\vec{r} - \vec{r}') \delta(t - t') \tag{1}$$

with speed of sound c . The boundary conditions can be written as

$$\frac{\partial G}{\partial \vec{r}} = 0 \text{ (zero normal velocity at the hard walls),} \tag{2a}$$

if G is taken to be a velocity potential. Also, the Green’s function satisfies the causality condition,

$$G(\vec{r}, \vec{r}', t - t')|_{t < t'} = 0 \text{ (no response before the impulse).} \tag{2b}$$

The solution of Eq. (1) and (2) is (see appendix A and [40])

$$G(\vec{r}, \vec{r}', t - t') = -\frac{1}{2\pi} \sum_{\substack{m,n,k=0 \\ (m,n,k) \neq (0,0,0)}}^{\infty} \frac{\varepsilon_m \varepsilon_n \varepsilon_k}{\Gamma_{mnk}} \psi_{mnk}(\vec{r}) \psi_{mnk}(\vec{r}') \int_{-\infty}^{\infty} \frac{e^{i\omega(t-t')}}{k_0^2 - k_{mnk}^2} d\omega, \tag{3}$$

where

$$\psi_{mnk}(\vec{r}) = \cos(k_x x) \cos(k_y y) \cos(k_z z) \tag{4}$$

are the (orthogonal) cavity eigenfunctions, with

$$k_x = \frac{m\pi}{H_x}, k_y = \frac{n\pi}{H_y} \text{ and } k_z = \frac{k\pi}{H_z}. \tag{5a,b,c}$$

k_x, k_y, k_z are the allowed wave numbers of the cavity, in the x, y and z direction, respectively, and m, n and k are the corresponding mode numbers; they can take values $0, 1, 2, \dots$, but they must not be zero simultaneously. Furthermore, the following abbreviations have been used in Eq. (3):

$$k_{mnk} = \sqrt{k_x^2 + k_y^2 + k_z^2} \text{ (magnitude of the allowed wave number vector),} \tag{6}$$

$$k_0 = \frac{\omega}{c} \text{ (wave number corresponding to the integration variable } \omega), \tag{7}$$

$$\varepsilon_m = \begin{cases} 1 & \text{if } m = 0 \\ 2 & \text{if } m > 0 \end{cases} \text{ (same for } \varepsilon_n \text{ and } \varepsilon_k), \tag{8}$$

$$\Gamma_{mnk} = H_x H_y H_z \text{ (volume integral of products of the eigenfunctions).} \tag{9}$$

The integral in Eq. (3) with respect to ω can be evaluated with the residue theorem, given that there are singularities in the integrand at $k_0 = \pm k_{mnk}$; the result is (see [40])

$$G(\vec{r}, \vec{r}', t - t') = c^2 \sum_{m,n,k=0}^{\infty} \frac{\varepsilon_m \varepsilon_n \varepsilon_k}{\omega_{mnk} \Gamma_{mnk}} \psi_{mnk}(\vec{r}) \psi_{mnk}(\vec{r}') \sin[\omega_{mnk}(t - t')], \tag{10}$$

where $\omega_{mnk} = ck_{mnk}$ are the allowed frequencies. Eq. (10) describes a superposition of modes, which is the expected response to a source in an acoustic resonator. A more convenient form of (10) is

$$G(\vec{r}, \vec{r}', t - t') = \sum_{m,n,k=0}^{\infty} g_{mnk}(\vec{r}, \vec{r}') \frac{1}{2} [e^{j\omega_{mnk}(t-t')} - e^{-j\omega_{mnk}(t-t')}], \tag{11}$$

with

$$g_{mnk}(\vec{r}, \vec{r}') = c^2 \frac{\varepsilon_m \varepsilon_n \varepsilon_k}{j \omega_{mnk} \Gamma_{mnk}} \psi_{mnk}(\vec{r}) \psi_{mnk}(\vec{r}'). \tag{12}$$

2.2. The heat release model

We assume that the flame is compact and located at the point $\vec{r} = \vec{r}_q$. We also assume that the flame is flat and that its surface normal is described by the angles φ and θ shown in Fig. 1. Its global heat release rate is described by a simple time-lag law, with coupling coefficient n and time-lag τ ,

$$\frac{Q'(t)}{\bar{Q}} = n \frac{u_r'(\vec{r}_q, t - \tau)}{\bar{u}_r}. \tag{13}$$

This equation relates the fluctuating part Q' of the heat release rate (normalized by the mean part \bar{Q}) to the component of the velocity that is normal to the flame surface. This component is denoted by a subscript r ; u_r' is the fluctuating part, and \bar{u}_r is the mean part of the normal acoustic velocity. The local equivalent of Eq. (13) is

$$q'(\vec{r}, t) = K_q n u_r(\vec{r}, t - \tau) \cdot \delta(\vec{r} - \vec{r}_q), \tag{14}$$

where q' is the heat release rate per unit mass (fluctuating part), the factor K_q stands for $K_q = \frac{\bar{Q}}{\bar{u}_r \bar{\rho}}$, and $\bar{\rho}$ is the mean density.

2.3. Derivation of the integral governing equation

The velocity potential $\phi(\vec{r}, t)$ of the sound field generated by a heat source can be described by the acoustic analogy equation [37]

$$\frac{1}{c^2} \frac{\partial^2 \phi}{\partial t^2} - \nabla^2 \phi = -\frac{\gamma - 1}{c^2} q'(\vec{r}, t). \tag{15}$$

Here, $\phi(\vec{r}, t)$ also has to satisfy the boundary conditions of zero normal velocity at the hard walls of the box,

$$\frac{\partial \phi}{\partial \vec{r}} = 0, \tag{16}$$

and the two initial conditions

$$\phi|_{t'=0} = \phi_0, \quad \left. \frac{\partial \phi}{\partial t'} \right|_{t'=0} = 0 \text{ at } \vec{r} = \vec{r}_q; \tag{17}$$

ϕ_0 in the first initial condition is the initial value of the velocity potential at the flame. For the second initial condition, we have chosen the value 0 for convenience.

With the tailored Green's function, this set of equations can be converted into an integral equation [37]:

$$\phi(\vec{r}, t) = -\frac{\gamma-1}{c^2} \int \int G(\vec{r}, \vec{r}', t-t') q'(\vec{r}', t') d\vec{r}' dt' - \left. \frac{\phi_0}{c^2} \left(\frac{\partial G}{\partial t'} \right) \right|_{\substack{t'=0 \\ \vec{r}' = \vec{r}_q}}. \tag{18}$$

This can be rewritten as an equation for the velocity u'_r by performing the following steps:

- substitute for $q'(\vec{r}', t')$ with Eq. (14)
- differentiate both sides of Eq. (18) with respect to the coordinate (denoted here by r) that is normal to the flame surface
- evaluate the resulting equation at the flame position, $\vec{r} = \vec{r}_q$
- replace $\left. \frac{\partial \phi(\vec{r}, t)}{\partial r} \right|_{\vec{r} = \vec{r}_q}$ by u'_q .

The resulting equation is

$$u'_q(t) = -\frac{\gamma-1}{c^2} K_q n \int_0^t \left(\frac{\partial G(\vec{r}, \vec{r}', t-t')}{\partial r} \right) \Big|_{\substack{\vec{r} = \vec{r}_q \\ \vec{r}' = \vec{r}_q}} u'_q(t'-\tau) dt' - \left. \frac{\phi_0}{c^2} \left(\frac{\partial^2 G}{\partial r \partial t'} \right) \right|_{\substack{t'=0 \\ \vec{r}' = \vec{r}_q}}. \tag{19}$$

This is a Volterra integral equation for the velocity at the flame. It relates $u'_q(t)$ at the observer time t to the velocity at earlier times, $u'_q(t'-\tau), t'=0, \dots, t$.

The flame-normal derivative $\frac{\partial}{\partial r}$ can be expressed in terms of cartesian coordinates,

$$\frac{\partial}{\partial r} = \frac{\partial x}{\partial r} \frac{\partial}{\partial x} + \frac{\partial y}{\partial r} \frac{\partial}{\partial y} + \frac{\partial z}{\partial r} \frac{\partial}{\partial z}, \tag{20}$$

where

$$\frac{\partial x}{\partial r} = \cos\varphi \sin\theta, \quad \frac{\partial y}{\partial r} = \sin\varphi \sin\theta, \quad \frac{\partial z}{\partial r} = \cos\theta \tag{21}$$

(from standard relationships between cartesian and spherical coordinates). The angles φ and θ are shown in Fig. 1. For the special case shown in Fig. 1(b), where there is no variation in the z -direction, (20) reduces to

$$\frac{\partial}{\partial r} = \cos\varphi \cdot \frac{\partial}{\partial x} + \sin\varphi \cdot \frac{\partial}{\partial y}. \tag{22}$$

2.4. Solutions of the integral governing equation

Eq. (19) governs the evolution of the acoustic field generated by the thermoacoustic feedback described above. In the following, two different methods are applied to solve this integral equation. The first one (Section 2.4.1) is a numerical iteration method, stepping forward in time; this gives the time history of the velocity fluctuations. The second one (Section 2.4.2) is an analytical approach, where we derive an algebraic equation for the complex eigenfrequency of the thermoacoustic system.

2.4.1. Time-stepping approach

The integral Eq. (19) is a Volterra equation of the second kind; it has the form

$$u(t) = \int_{t'=0}^t K(t, t') u(t'-\tau) dt' + f(t), \tag{23}$$

where $u(t)$ is the function to be solved for,

$$K(t, t') = -\frac{\gamma-1}{c^2} K_q n \left(\frac{\partial G(\vec{r}, \vec{r}', t-t')}{\partial r} \right) \Bigg|_{\substack{\vec{r} = \vec{r}_q \\ \vec{r}' = \vec{r}'_q}} \quad (24)$$

is the integral kernel, and

$$f(t) = -\frac{\phi_0}{c^2} \left(\frac{\partial^2 G}{\partial r \partial t'} \right) \Bigg|_{\substack{t' = 0 \\ \vec{r} = \vec{r}_q \\ \vec{r}' = \vec{r}'_q}} \quad (25)$$

is the non-homogeneous term. The iterative solution of a standard Volterra equation is known and can be found e.g. in chapter 19 [41]. The approach basically involves discretising the time variables t and t' , and then applying the trapezoidal rule to the integral. However, in our case, the integrand contains the time-lag τ , and this makes it necessary to modify the approach. A detailed description can be found in [appendix B](#). Here, we just give a summary of the key equations.

The variables t and t' are discretised by

$$t_N = Nh, \quad N = 0, 1, 2, \dots, \quad (26)$$

where h is the (constant) time-step. Correspondingly, the time-lag τ is treated as a discrete quantity, which may take values

$$\tau = Mh, \quad (27)$$

where M is a fixed natural number.

The iteration scheme proceeds as follows. For the first few iteration steps, until t_N becomes equal to the time-lag, the equations are simply

$$N = 0, 1, \dots, M : u(t_N) = f(t_N). \quad (28a)$$

For the next two iteration steps, we have

$$N = M + 1 : u(t_N) = f(t_N) + \frac{h}{2} [K(t_N, t_M)u(t_0) + K(t_N, t_N)u(t_1)], \quad (28b)$$

$$N = M + 2 : u(t_N) = f(t_N) + \frac{h}{2} [K(t_N, t_M)u(t_0) + K(t_N, t_N)u(t_2)] + hK(t_N, t_{M+1})u(t_1). \quad (28c)$$

For all subsequent iteration steps, $N > M + 2$:

$$u(t_N) = f(t_N) + \frac{h}{2} [K(t_N, t_M)u(t_0) + K(t_N, t_N)u(t_{N-M})] + h \sum_{i=M}^{N-2} K(t_N, t_{i+1})u(t_{i-M+1}). \quad (28d)$$

The initial condition (17) is contained in the non-homogeneous term f (see [Eq. \(25\)](#)) and affects the result at every iteration step.

2.4.2. Calculation of the thermoacoustic eigenfrequencies

This method is based on the observation that the thermoacoustic field in a resonator is a superposition of modes. We express this mathematically by writing the acoustic velocity as a sum of modes with complex amplitudes $u_{\mu\nu\kappa}$ and complex frequencies $\Omega_{\mu\nu\kappa}$,

$$u'_q(t) = \sum_{\mu\nu\kappa} u_{\mu\nu\kappa} e^{j\Omega_{\mu\nu\kappa} t}. \quad (29)$$

It is not necessary to take only the real part of (29); this is because (19) is a linear equation in u'_q , and the Green's function as well as the other quantities in this equation are real. At this stage, $u_{\mu\nu\kappa}$ and $\Omega_{\mu\nu\kappa}$ are unknown. It is possible to determine them from a series of mathematical manipulations, based on the integral [Eq. \(19\)](#) and [Eq. \(10\)](#) for $G(\vec{r}, \vec{r}', t-t')$. Details of the derivation can be found in [Appendix C](#). The resulting equations are

$$1 = -\frac{\gamma-1}{c^2} K_q n e^{-j\Omega_{\mu\nu\kappa} \tau} \sum_{mnk} \frac{1}{2} G_{mnk} \left[\frac{1}{j(-\omega_{mnk} + \Omega_{\mu\nu\kappa})} - \frac{1}{j(\omega_{mnk} + \Omega_{\mu\nu\kappa})} \right] \quad (30)$$

and

$$-\frac{\gamma-1}{c^2} K_q n \sum_{\mu\nu\kappa} \frac{e^{-j\Omega_{\mu\nu\kappa} \tau}}{j(-\omega_{mnk} + \Omega_{\mu\nu\kappa})} u_{\mu\nu\kappa} = \frac{\phi_0}{c^2} j\omega_{mnk}, \quad (31)$$

where G_{mnk} is the gradient of the Green's function amplitude (see Eq. (C4)). Eq. (30) is an equation for the frequencies $\Omega_{\mu\nu\kappa}$. Once this has been solved for $\Omega_{\mu\nu\kappa}$, the solution can be put into (31) to obtain the solution for the velocity amplitude $u_{\mu\nu\kappa}$. The imaginary part of $\Omega_{\mu\nu\kappa}$ gives the stability behaviour of the thermoacoustic mode $\mu\nu\kappa$.

For the case, where the Green's function is dominated by a single mode mnk , the Eqs. (30) and (31) can be simplified by dropping the sum. The equation resulting from (30) can then be written as

$$\Omega_{\mu\nu\kappa}^2 - \omega_{mnk}^2 - \frac{\gamma - 1}{c^2} K_q n 2j\omega_{mnk} G_{mnk} e^{-j\Omega_{\mu\nu\kappa}\tau} = 0. \tag{32}$$

In general, this equation has two roots. It is easy to show that if Ω is one of the roots, then $-\Omega^*$ must be the other root.

3. Model validation

3.1. Comparison with a 1-D network model

In order to test the model developed in Section 2, we consider the mode $(m, n, k) = (1, 0, 0)$ in isolation. For this mode, the acoustic field varies only along the x -axis, but not along the y or z -axis. In other words, we reduce our model to a 1-D situation, which can also be analysed by a simple 1-D network model. Fig. 2 shows the relevant geometry.

A duct of length L , with both ends closed, represents the 1-D cavity. An infinitesimally thin flame sheet, spanning the duct's cross-section, is located at $x = x_q$. The temperature is uniform throughout the duct; the mean density is $\bar{\rho}$.

1-D acoustic waves propagate in the positive and negative x -direction on either side of the flame. The corresponding pressure and velocity fields are given by

$$\hat{p}(x) = \begin{cases} Ae^{-j\frac{\Omega}{c}(x-x_q)} + Be^{j\frac{\Omega}{c}(x-x_q)} & \text{for } 0 \leq x < x_q \\ Ce^{-j\frac{\Omega}{c}(x-x_q)} + De^{j\frac{\Omega}{c}(x-x_q)} & \text{for } x_q < x \leq L \end{cases} \tag{33}$$

$$\hat{u}(x) = \frac{1}{\bar{\rho}c} \begin{cases} -Ae^{-j\frac{\Omega}{c}(x-x_q)} + Be^{j\frac{\Omega}{c}(x-x_q)} & \text{for } 0 \leq x < x_q \\ -Ce^{-j\frac{\Omega}{c}(x-x_q)} + De^{j\frac{\Omega}{c}(x-x_q)} & \text{for } x_q < x \leq L \end{cases} \tag{34}$$

The superscript $\hat{}$ denotes complex amplitudes. At this stage, A, B, C and D are unknown pressure amplitudes. They are related by the following jump conditions across the flame at $x = x_q$:

$$\hat{p}(x_q^+) - \hat{p}(x_q^-) = 0, \tag{35a}$$

$$\hat{u}(x_q^+) - \hat{u}(x_q^-) = \frac{\gamma - 1}{c^2} \hat{Q}, \tag{35b}$$

where \hat{Q} is the complex amplitude of $Q'(t)$. It can be readily obtained by Fourier transform of (13),

$$\hat{Q} = K_q n \hat{u}(x_q^-) e^{-j\Omega\tau}, \tag{36}$$

where K_q is the constant factor introduced just after Eq. (14).

The unknown pressure amplitudes are also related by the hard-wall boundary conditions at $x = 0$ and $x = L$, which are described by the pressure reflection coefficients

$$R_0 = 1 \text{ and } R_L = 1; \tag{37}$$

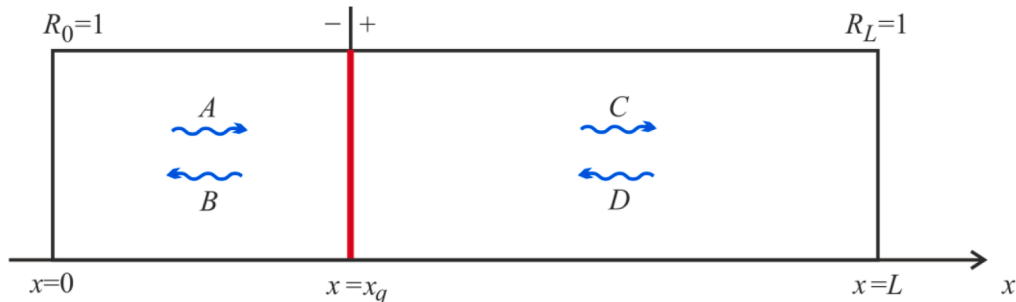


Fig. 2. Schematic of the 1-D situation.

this gives

$$A = B e^{-2j\frac{\Omega}{c}x_q}, \quad (38a)$$

$$D = C e^{-2j\frac{\Omega}{c}(L-x_q)}. \quad (38b)$$

Altogether, we have 4 equations for the 4 unknowns A, B, C and D : Eqs. (38a), (38b), (35a) (with \hat{p} replaced by (33)), and (35b) (with \hat{Q} replaced by (36) and \hat{u} by (34)). They form a linear homogeneous set of equations, which can be written in terms of a 4×4 matrix. For non-zero solutions to exist, the determinant of the 4×4 matrix must be zero. This condition leads to a nonlinear equation for the thermoacoustic eigenfrequency Ω . This is called the characteristic equation, and it reads

$$2 - 2e^{-2j\frac{\Omega}{c}L} + \frac{\gamma - 1}{c^2} K_q n e^{-j\Omega\tau} \left[e^{-2j\frac{\Omega}{c}(L-x_q)} + 1 - e^{-2j\frac{\Omega}{c}L} - e^{-2j\frac{\Omega}{c}x_q} \right] = 0. \quad (39)$$

Eq. (39) was solved for Ω with the Newton-Raphson method for a range of τ values and x_q values.

Fig. 3 shows Ω as a function of τ : $\text{Re}(\Omega)$ is shown in part (a), and $\text{Im}(\Omega)$ in part (b). The black curves give the results of the network model (obtained from Eq. (39)), while the red curves give the results of the Green's function method (determined from the time history which was obtained by solving the integral Eq. (19) as described in Section 2.4.1. It is evident from a comparison of these curves that the agreement is very good.

In a similar vein, Fig. 4 shows Ω as a function of x_q . Again, the agreement between the results of the two methods is very good.

3.2. Comparison of approach based on thermoacoustic eigenfrequencies with time-stepping approach

In order to test the calculation of the thermoacoustic eigenfrequencies developed in Section 2.4.2, we consider the 2-D situation of a rectangular cavity with side lengths H_x, H_y , and a flame angle $\varphi = 45^\circ$. The comparison is done in terms of time histories, which are calculated in two ways: (1) by the time-stepping approach described in Section 2.4.1, and (2) by evaluating Eq. (29) with the thermoacoustic eigenfrequencies $\Omega_{\mu\nu k}$ from (30) and the corresponding amplitudes $u_{\mu\nu k}$ from (31).

Two scenarios are considered and shown in Fig. 5. The first (see Fig. 5(a)) is a square cavity with side lengths $H_x = H_y = 1$ m and a single mode $(m, n, k) = (1, 1, 0)$. The second (see Fig. 5(b)) is a rectangular cavity with side lengths $H_x = 1$ m, $H_y = 1.2$ m and the two modes $(m, n, k) = (1, 0, 0)$ and $(0, 1, 0)$. The red curves give the results of the approach based on the thermoacoustic eigenfrequencies, while the black curves give the results of the time-stepping approach. The red curves lie directly on top of the black curves, indicating excellent agreement.

4. Results and discussion for a single-frequency resonator

In order to understand the key features of any thermoacoustic instabilities, we consider a 2-D resonator (equivalent to a 3-D resonator with mode number $k = 0$) with a 2-D flame inside. The resonator is a square with $H_x = H_y = 1$ m. The first modal frequency in the two directions is the same, i.e. $\omega_{100} = \omega_{010} = 1068 \text{ s}^{-1}$. The second modal frequency is $\omega_{110} = 1511 \text{ s}^{-1}$. We consider this second frequency on its own for the remainder of this section; the case of two frequencies will be treated in Section 5.

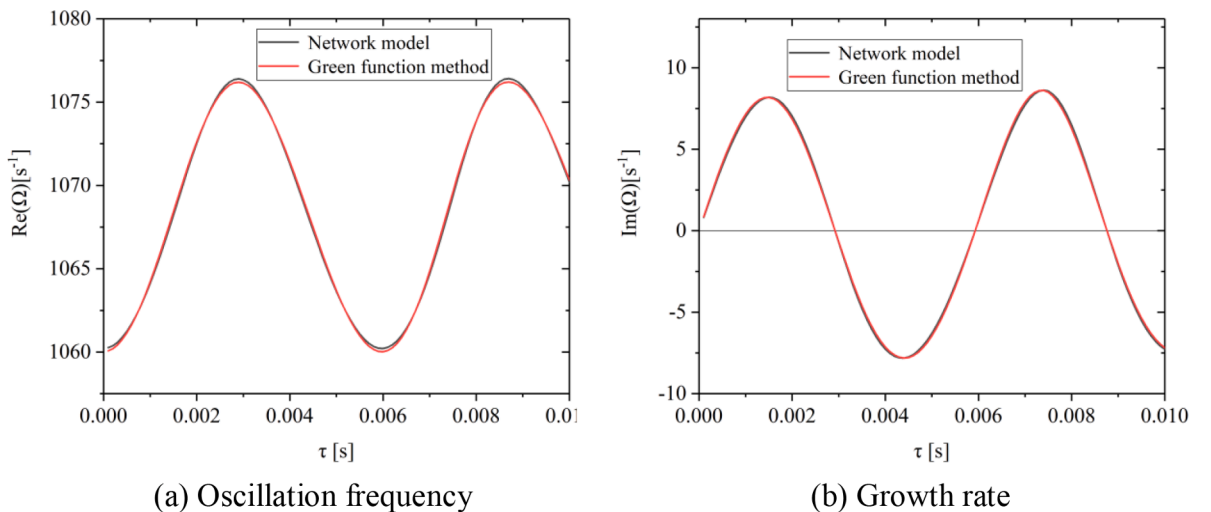


Fig. 3. Comparison of the τ -dependence of the thermoacoustic eigenfrequency calculated from the Green's function method (red curve) and from the network model (black curve). The flame is located at $x_q = 0.2$ m; the other parameters are $L = 1$ m (length of duct), $c = 340 \text{ ms}^{-1}$ (speed of sound), $K_q n = 1.45 \times 10^4 \text{ W m}^2 \text{ s kg}^{-1}$ (power of flame); (a) real part (oscillation frequency), (b) imaginary part (growth rate).

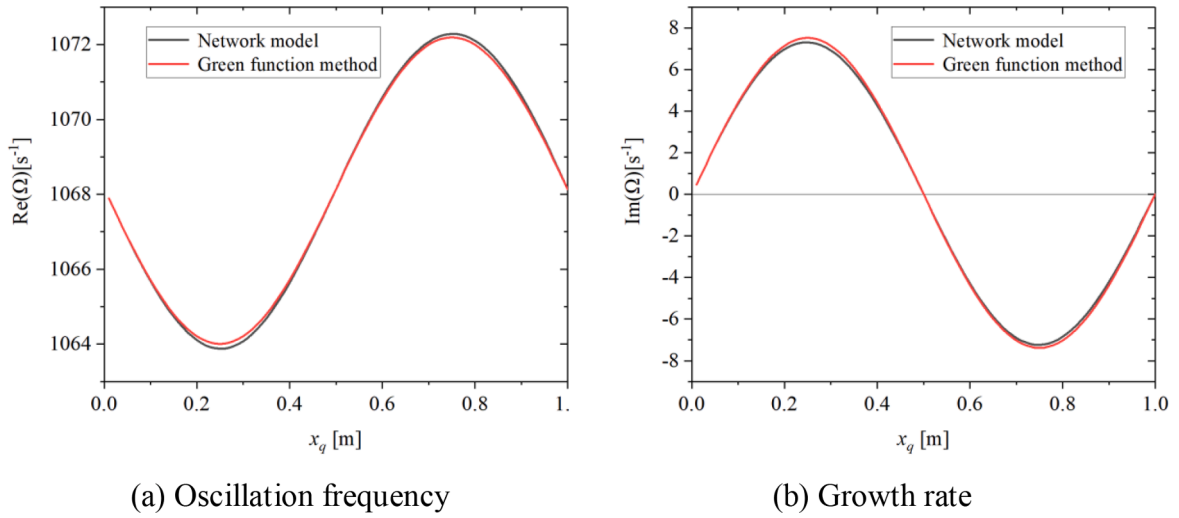


Fig. 4. Comparison of the x_q -dependence of the thermoacoustic eigenfrequency calculated from the Green’s function method (red curve) and from the network model (black curve). The time-lag is $\tau = 0.001$ s; the other parameters are $L = 1$ m, $c = 340$ ms $^{-1}$, $K_q n = 1.45 \times 10^4$ W m 2 s kg $^{-1}$; (a) real part (oscillation frequency), (b) imaginary part (growth rate).

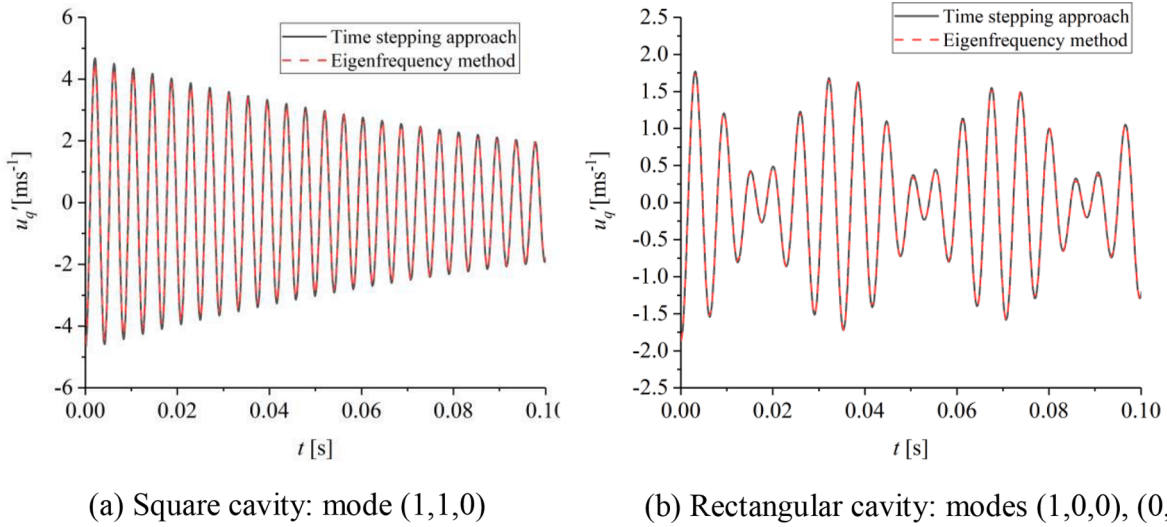


Fig. 5. Comparison of the time histories calculated from the approach based on the thermoacoustic eigenfrequencies (red curves) and the time-stepping approach (black curves). The parameters for the flame characteristics are $x_q = 0.1$ m, $y_q = 0.1$ m, $\varphi = 45^\circ$, $\tau = 0.001$ s, $K_q n = 1.45 \times 10^4$ W m 2 s kg $^{-1}$; (a) square cavity ($H_x = H_y = 1$ m) with single mode (1,1,0), (b) rectangular cavity ($H_x = 1$ m, $H_y = 1.2$ m) with two modes (1,0,0) and (0,1,0).

4.1. Influence of the flame angle and flame position

First, we move the flame along the x -axis (while keeping y_q constant) and calculate the complex thermoacoustic eigenfrequencies $\Omega_{\mu\nu\kappa}$ from Eq. (30) for the following three flame angles: $\varphi = 0$, $\varphi = 45^\circ$ and $\varphi = 120^\circ$. The results are shown in Fig. 6: part (a) shows the oscillation frequency, $\text{Re}(\Omega)$, and part (b) shows the growth rate, $\text{Im}(\Omega)$.

We observe from Fig. 6(b) that for $\varphi = 0$ (black curve), the x_q -range is divided into two equal parts: there is stability in the first half ($0 < x_q < 0.5$ m), and instability in the second half ($0.5 < x_q < 1$ m). For the other two angles, $\varphi = 45^\circ$ (red curve) and $\varphi = 120^\circ$ (blue curve), the stable range along the x -axis is larger than that for $\varphi = 0$. This is a new phenomenon (in the sense that it cannot be captured by 1-D models), which is caused by the fact that the flame is angled.

Next we move the flame along a diagonal path through the box. Again, we calculate the complex thermoacoustic eigenfrequencies $\Omega_{\mu\nu\kappa}$ from Eq. (30). The results are shown in Figs. 7(a) and 7(b) for the two flame angles: $\varphi = 0$ (black curve), and $\varphi = 45^\circ$ (red curve). Part (a) shows the oscillation frequency, $\text{Re}(\Omega)$, and part (b) shows the growth rate, $\text{Im}(\Omega)$. r_q is the distance of the flame from the

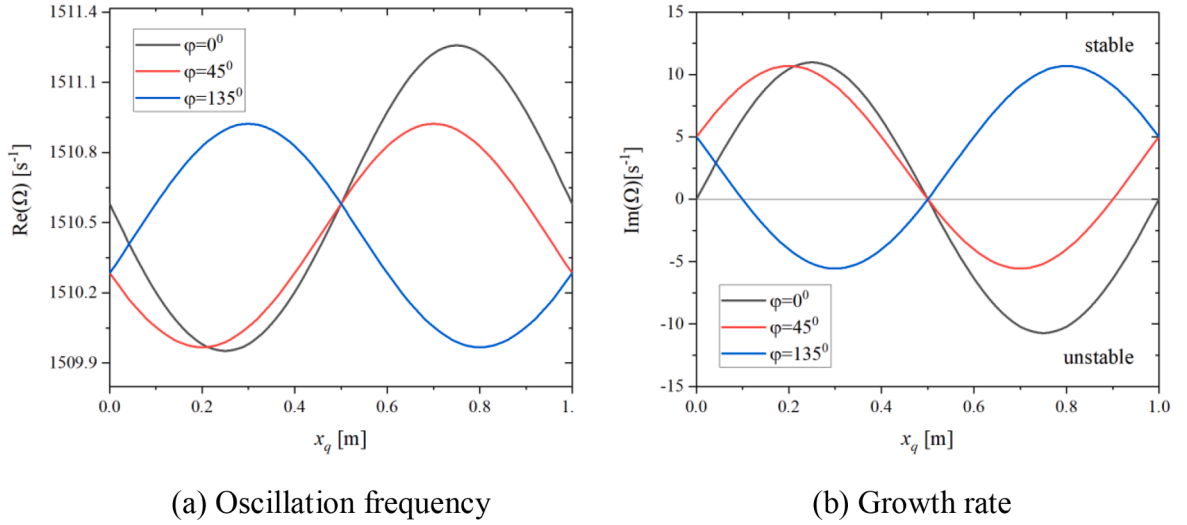


Fig. 6. Thermoacoustic eigenfrequency as a function of flame position along the x-axis for three flame angles φ . The other parameters are $H_x = H_y = 1$ m, $y_q = 0.1$ m, $\tau = 0.001$ s, $K_q n = 1.45 \times 10^4$ W m 2 s kg $^{-1}$; the mode number is (1,1,0); (a) real part (oscillation frequency), (b) imaginary part (growth rate).

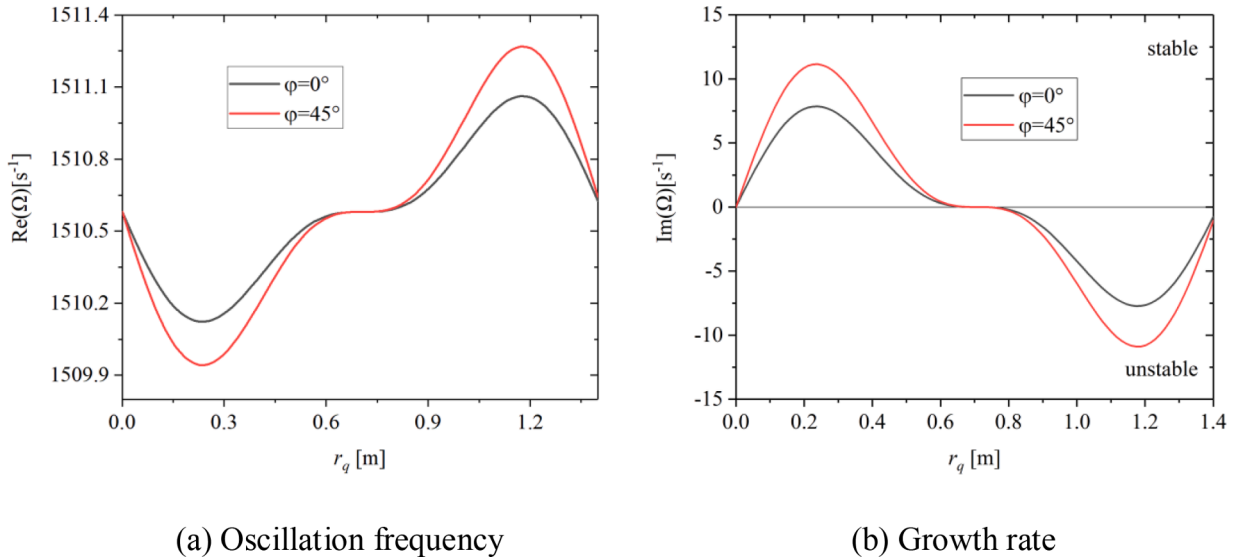


Fig. 7. Thermoacoustic eigenfrequency as a function of flame position along the diagonal line (from the bottom left to the top right corner) for two flame angles φ . The other parameters are $H_x = H_y = 1$ m, $\tau = 0.001$ s, $K_q n = 1.45 \times 10^4$ W m 2 s kg $^{-1}$; the mode number is (1,1,0); (a) real part (oscillation frequency), (b) imaginary part (growth rate).

origin and ranges from 0 to $\sqrt{2}$ m in a box of 1 m \times 1 m.

We observe from Fig. 7(b) that there is stability along the first half of the flame path (i.e. while the flame is in the bottom left quarter of the box) and instability along the second half of the path (i.e. while the flame is in the top right quarter of the box). There is a relatively large region halfway along the path, where $\text{Im}(\Omega)$ is very close to zero; this indicates that the transition from stable to unstable is very gradual. Again this is a new phenomenon, and it is caused by the fact that the acoustic field in the box is 2-D.

4.2. Interpretation in terms of the Rayleigh index

In order to understand this in detail, we consider the local Rayleigh index [42]

$$RI = \overline{p'(x, y, t)Q'(t)} \Big|_{y=y_q}^{x=x_q}, \quad (40)$$

where the overbar denotes the time average over one oscillation period, and the dashes denote time-domain quantities. If RI is positive, the system is unstable; otherwise it is stable. The sign of RI , and therefore the stability behaviour, depend critically on the phase difference between $p'(x_q, y_q, t)$ and $Q'(t)$. The acoustic pressure is given by (see chapter 9 in [43])

$$p'(x, y, t) = P_0 f_p(x, y) \cos \omega t, \tag{41}$$

and the momentum equation then gives the acoustic velocity as

$$u_r'(x, y, t) = \frac{P_0}{\rho c} f_u(x, y, \varphi) \sin \omega t, \tag{42}$$

where $f_p(x, y)$ and $f_u(x, y, \varphi)$ are distribution functions, defined by

$$f_p(x, y) = \cos\left(\frac{\pi x}{H_x}\right) \cos\left(\frac{\pi y}{H_y}\right), \tag{43}$$

$$f_u(x, y, \varphi) = \sin\left(\frac{\pi x}{H_x}\right) \cos\left(\frac{\pi y}{H_y}\right) \cos \varphi + \cos\left(\frac{\pi x}{H_x}\right) \sin\left(\frac{\pi y}{H_y}\right) \sin \varphi, \tag{44}$$

and P_0 is the pressure amplitude. Given that Q' is proportional to the time-lagged velocity $u_r'(x_q, y_q, t - \tau)$ (see Eq. (13)), we can write

$$Q'(t) = K_q n \frac{P_0}{\rho c} f_u(x_q, y_q, \varphi) \sin \omega(t - \tau). \tag{45}$$

The phase differences between these three quantities are illustrated in Fig. 8 for the special case $\varphi = 0$, where $p'(x_q, y_q, t)$ (black curves), $u_r'(x_q, y_q, t)$ (red curves) and $Q'(t)$ (blue curves) have been plotted as functions of time over one period. In Fig. 8(a), the phase difference between p' and u_r' is $+90^\circ$, and the phase difference between p' and Q' is between 90° and 180° , so the Rayleigh index is negative. In Fig. 8(b), the phase difference between p' and u_r' is -90° , and that between p' and Q' is between -90° and 0° , so the Rayleigh index is positive.

The key parameters are the flame angle φ , the flame position (x_q, y_q) , and the time-lag τ . In order to investigate their influence in a systematic fashion, we rewrite RI with (41) and (45), and by using the time averages $\overline{\cos \omega t \sin \omega t} = 0$, $\overline{\cos \omega t \sin \omega(t - \tau)} = -\frac{1}{2} \sin \omega \tau$. The result is

$$RI = -\frac{1}{2} K_q n \frac{P_0^2}{\rho c} \sin \omega \tau f_p(x, y) f_u(x, y, \varphi). \tag{46}$$

The term $\frac{1}{2} K_q n \frac{P_0^2}{\rho c}$ is a positive constant; the sign of RI therefore depends on the following three quantities: $\sin \omega \tau, f_p(x, y), f_u(x, y, \varphi)$.

For moderately small values of τ (i.e. $\tau \in \left[0, \frac{T}{2}\right]$, so that $\sin \omega \tau > 0$), the sign of the product

$$f_{pu}(x, y, \varphi) = -f_p(x, y) f_u(x, y, \varphi) \tag{47}$$

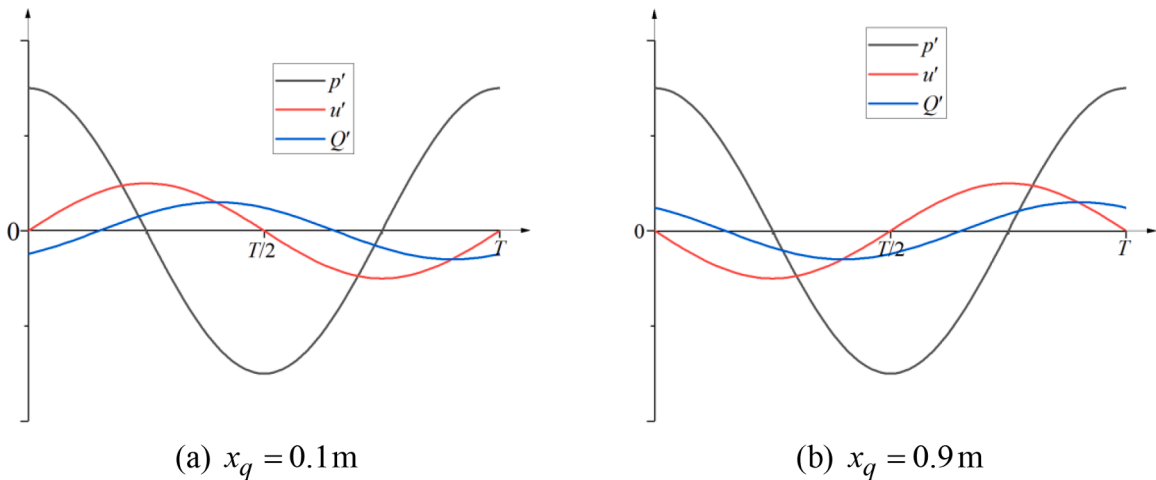


Fig. 8. One cycle of the time history of $p'(x_q, y_q, t)$, $u_r'(x_q, y_q, t)$ and $Q'(t)$ at the flame position. In both parts of the figure, $y_q = 0.1$ m (bottom half of box), $\varphi = 0$, $K_q n = 1.45 \times 10^4$ W m² s kg⁻¹ and $H_x = H_y = 1$ m; (a) $x_q = 0.1$ m (left half of box), (b) $x_q = 0.9$ m (right half of box).

determines the stability behaviour. With (43) and (44), this can be written as

$$f_{pu}(x, y, \varphi) = -\frac{1}{2} \sin\left(\frac{2\pi x}{H_x}\right) \cos^2\left(\frac{\pi y}{H_y}\right) \cos\varphi - \frac{1}{2} \sin\left(\frac{2\pi y}{H_y}\right) \cos^2\left(\frac{\pi x}{H_x}\right) \sin\varphi. \tag{48}$$

The x - and y -dependence of the individual terms is shown schematically in Fig. 9.

Clearly, $f_{pu} = 0$ for any φ if $x = \frac{1}{2}H_x$ or $y = \frac{1}{2}H_y$. This indicates that the box, which has side lengths H_x and H_y , is divided into four quarters. We can draw further conclusions by considering the two flame angle ranges $0 < \varphi < 90^\circ$ (where $\sin\varphi > 0, \cos\varphi > 0$), and $90^\circ < \varphi < 180^\circ$ (where $\sin\varphi > 0, \cos\varphi < 0$) separately, starting with the first range.

- (1) $f_{pu} < 0$ for $0 < \varphi < 90^\circ$ if $x \in \left[0, \frac{1}{2}H_x\right]$ and $y \in \left[0, \frac{1}{2}H_y\right]$.
- (2) $f_{pu} > 0$ for $0 < \varphi < 90^\circ$ if $x \in \left[\frac{1}{2}H_x, H_x\right]$ and $y \in \left[\frac{1}{2}H_y, H_y\right]$.
- (3) $f_{pu} = 0$ for $\varphi = 45^\circ$ if $H_x = H_y$ (square box) and $y = -x + H_y$ (diagonal line from top left to bottom right).

Fig. 10 shows the stability maps for the three angles $\varphi = 0, \varphi = 45^\circ$ and $\varphi = 90^\circ$; stable regions are blue and unstable regions are red.

The sign in the bottom left quarter is always negative, and that in the top right quarter is always positive. However, the sign in the other two quarters depends very much on the angle φ . In fact, these two quarters have a uniform sign if $\varphi = 0$ or $\varphi = 90^\circ$, but not for the angle $\varphi = 45^\circ$. For this angle, these quarters are divided into a positive and negative region.

In order to investigate the transition from $\varphi = 0$ to 45° , and from $\varphi = 45^\circ$ to 90° , we consider the two angles $\varphi = 0 + \varepsilon$ and $\varphi = 90^\circ - \varepsilon$, where ε is a small angle.

For $\varphi = 0 + \varepsilon$, f_{pu} in Eq. (48) becomes with $\cos\varphi \approx 1$ and $\sin\varphi \approx \varepsilon$

$$f_{pu}(x, y, \varphi) = -\frac{1}{2} \sin\left(\frac{2\pi x}{H_x}\right) \cos^2\left(\frac{\pi y}{H_y}\right) - \frac{1}{2} \varepsilon \sin\left(\frac{2\pi y}{H_y}\right) \cos^2\left(\frac{\pi x}{H_x}\right). \tag{49}$$

The first term is equal to $f_{pu}|_{\varphi=0}$, and the much smaller second term can be seen as a "perturbation" of the case $\varphi = 0$. From the sign of the second term,

$$-\frac{1}{2} \varepsilon \sin\left(\frac{2\pi y}{H_y}\right) \cos^2\left(\frac{\pi x}{H_x}\right) \begin{cases} < 0 & \text{for } y \in \left[0, \frac{1}{2}H_y\right] \\ > 0 & \text{for } y \in \left[\frac{1}{2}H_y, H_y\right] \end{cases} \tag{50}$$

we conclude that with increasing ε , the negative region in the top left quarter becomes smaller, as well as the positive region in the bottom right quarter. A sketch is shown in Fig. 11(a).

For $\varphi = 90^\circ - \varepsilon$, f_{pu} in Eq. (48) becomes with $\cos\varphi \approx \varepsilon$ and $\sin\varphi \approx 1$

$$f_{pu}(x, y, \varphi) = -\frac{1}{2} \cos^2\left(\frac{\pi x}{H_x}\right) \sin\left(\frac{2\pi y}{H_y}\right) - \frac{1}{2} \varepsilon \sin\left(\frac{2\pi x}{H_x}\right) \cos^2\left(\frac{\pi y}{H_y}\right). \tag{51}$$

Again, the first term is equal to $f_{pu}|_{\varphi=90^\circ}$, and the much smaller second term can be seen as a "perturbation", now of the case $\varphi = 90^\circ$. The sign of the second term,

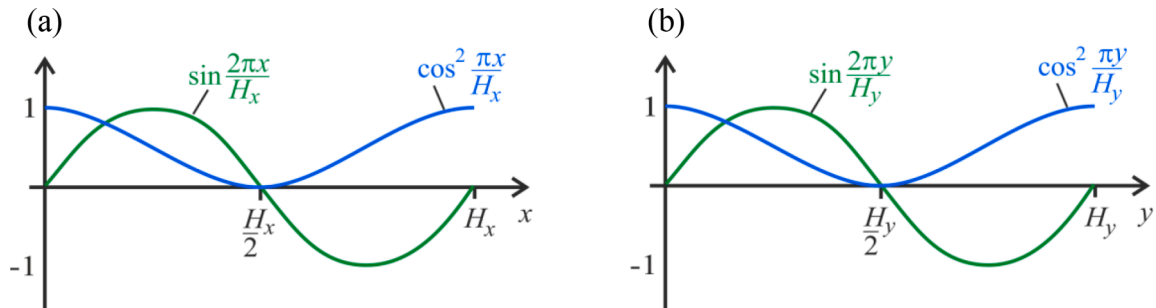


Fig. 9. Individual terms in Eq. (48); (a) x -dependence, (b) y -dependence.

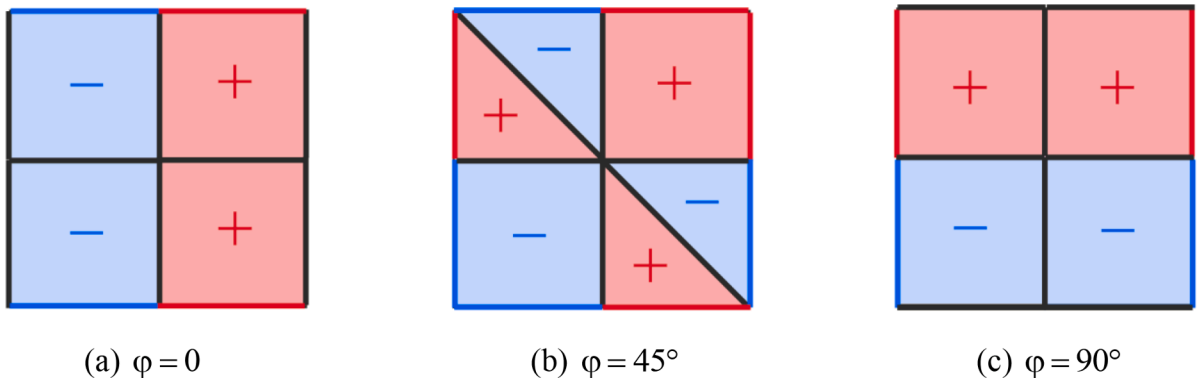


Fig. 10. Stability maps for a square box; (a) $\varphi = 0$, (b) $\varphi = 45^\circ$, (c) $\varphi = 90^\circ$.

— lines of $f_{pu} < 0$, — regions of $f_{pu} < 0$ (stable),
 — lines of $f_{pu} > 0$, — regions of $f_{pu} > 0$ (unstable),
 — lines of $f_{pu} = 0$.

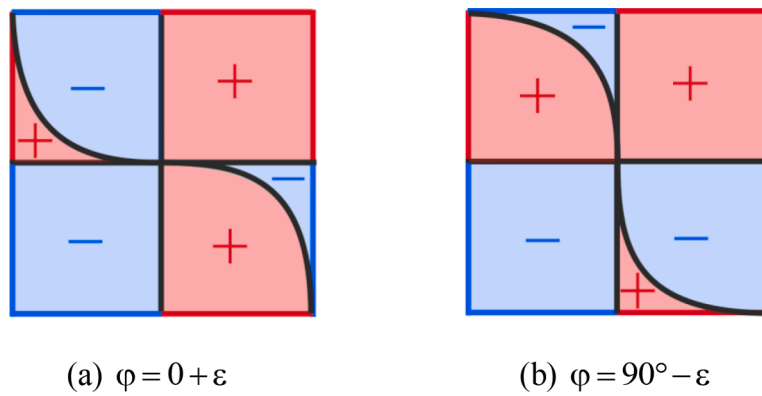


Fig. 11. Stability maps for a square box; (a) $\varphi = 0 + \varepsilon$, (b) $\varphi = 90^\circ - \varepsilon$.

— lines of $f_{pu} < 0$, — regions of $f_{pu} < 0$ (stable),
 — lines of $f_{pu} > 0$, — regions of $f_{pu} > 0$ (unstable),
 — curves of $f_{pu} = 0$.

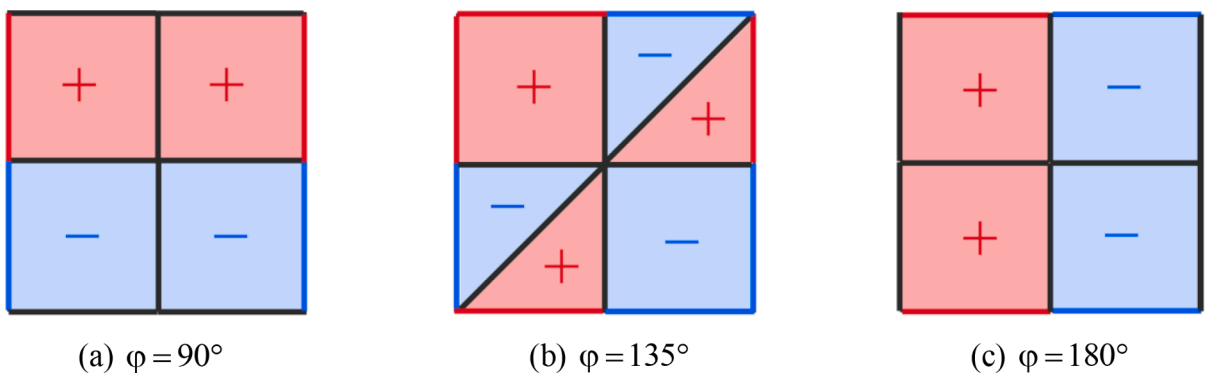


Fig. 12. Stability maps for a square box; (a) $\varphi = 90^\circ$, (b) $\varphi = 135^\circ$, (c) $\varphi = 180^\circ$.

— lines of $f_{pu} < 0$, — regions of $f_{pu} < 0$ (stable),
 — lines of $f_{pu} > 0$, — regions of $f_{pu} > 0$ (unstable),
 — lines of $f_{pu} = 0$.

$$-\frac{1}{2}\varepsilon\sin\left(\frac{2\pi x}{H_x}\right)\cos^2\left(\frac{\pi y}{H_y}\right)\begin{cases} < 0 \text{ for } x \in \left[0, \frac{1}{2}H_x\right] \\ > 0 \text{ for } x \in \left[\frac{1}{2}H_x, H_x\right] \end{cases} \tag{52}$$

indicates that with increasing ε , the positive region in the top left quarter becomes smaller, as well as the negative region in the bottom right quarter. A sketch is shown in Fig. 11(b).

We now draw conclusions for the flame angle range $90^\circ < \varphi < 180^\circ$.

- (1) $f_{pu} < 0$ for $90^\circ < \varphi < 180^\circ$ if $x \in \left[\frac{1}{2}H_x, H_x\right]$ and $y \in \left[0, \frac{1}{2}H_y\right]$.
- (2) $f_{pu} > 0$ for $90^\circ < \varphi < 180^\circ$ if $x \in \left[0, \frac{1}{2}H_x\right]$ and $y \in \left[\frac{1}{2}H_y, H_y\right]$.
- (3) $f_{pu} = 0$ for $\varphi = 45^\circ$ if $H_x = H_y$ (square box) and $y = x$ (diagonal line from bottom left to top right).

Fig. 12 shows the stability maps for the three angles $\varphi = 90^\circ$, $\varphi = 135^\circ$ and $\varphi = 180^\circ$.

The sign in the top left quarter is always positive and that in the bottom right quarter is always negative. However, the sign in the other two quarters depends very much on the angle φ , and it is again worthwhile examining the transition by performing the "perturbation" analysis shown above, but now for $\varphi = 90^\circ + \varepsilon$ and $\varphi = 180^\circ - \varepsilon$. The results are shown in Fig. 13.

The above considerations were based on the assumption that $\sin\omega\tau > 0$, which is the case if τ is in the range $\left[0, \frac{T}{2}\right]$. If τ is such that $\sin\omega\tau < 0$, which happens for $\tau \in \left[\frac{T}{2}, T\right]$, the patterns shown in Figs. 10–13 remain, but the regions of instability now correspond to $f_{pu} < 0$ and regions of stability to $f_{pu} > 0$.

4.3. Quantitative stability maps from numerical calculation of the thermoacoustic eigenfrequencies

We complement the qualitative results of the previous section by showing stability maps produced by calculating the thermoacoustic eigenfrequencies Ω_{110} (as described in Section 2.4.2) and deducing the stability behaviour from the sign of $\text{Im}(\Omega_{110})$. Our configuration here is a square box of $1\text{ m} \times 1\text{ m}$, which houses a flame described by $\tau = 0.001\text{ s}$ (this is in the range $\left[0, \frac{T}{2}\right]$) and $K_q n = 1.45 \times 10^4\text{ W m}^2\text{ s kg}^{-1}$; the mode number is (1,1,0). Fig. 14 shows contour maps of the growth rate $\text{Im}(\Omega_{110})$ for the flame angles considered in Figs. 10 and 12 of the previous section.

Figs. 14(a)–(c) correspond to Figs. 10(a)–(c), while Figs. 14(d) and (e) correspond to 12 (b) and (c). It is evident that the corresponding figures are fully consistent.

In Fig. 15 below, we show contour maps for the neighbouring φ -values 5° , 85° , 95° and 175° .

These angles have been chosen because they allow comparison with the qualitative stability maps in Figs. 11 and 13. Fig. 11(a), which shows the stability map for $\varphi = 0 + \varepsilon$, corresponds to Fig. 15(a), where $\varphi = 5^\circ$ (i.e. $\varepsilon = 5^\circ$). Likewise, Fig. 11(b), which shows the stability map for $\varphi = 90^\circ - \varepsilon$, corresponds to Fig. 15(b), where $\varphi = 90^\circ - 5^\circ = 85^\circ$. Again, it is evident that the corresponding figures are fully consistent. It is the same story for the two angles $\varphi = 90^\circ + 5^\circ = 95^\circ$ (compare Figs. 13(a) and 15(c)) and $\varphi = 180^\circ - 5^\circ = 175^\circ$ (compare Figs. 13(b) and 15(d)).

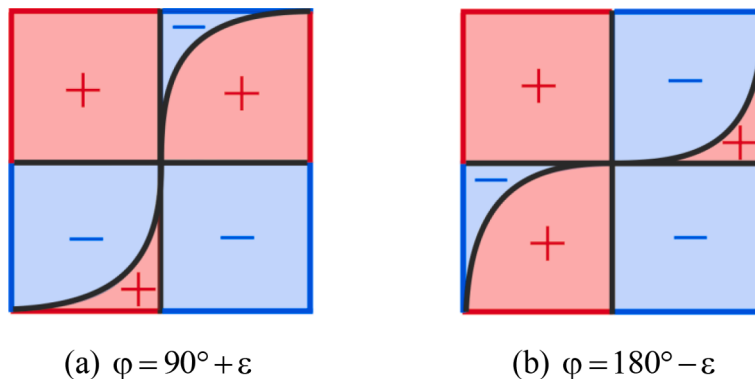


Fig. 13. Stability maps for a square box; (a) $\varphi = 90^\circ + \varepsilon$, (b) $\varphi = 180^\circ - \varepsilon$.

- lines of $f_{pu} < 0$, — regions of $f_{pu} < 0$ (stable),
- lines of $f_{pu} > 0$, — regions of $f_{pu} > 0$ (unstable),
- curves of $f_{pu} = 0$.

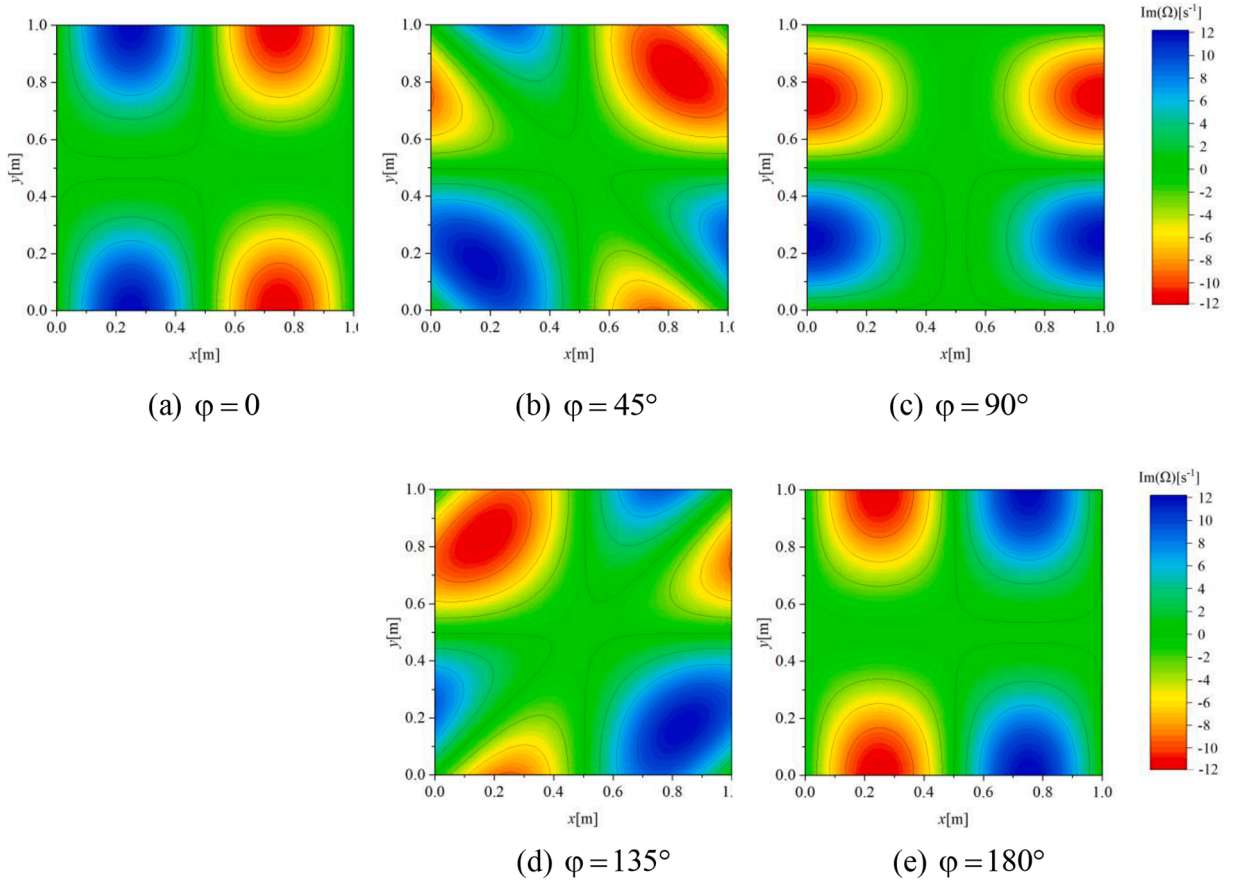


Fig. 14. Contour maps of the growth rate $\text{Im}(\Omega_{110})$ for a square box with side lengths $H_x = H_y = 1$ m, containing a flame with $\tau = 0.001$ s and $K_f n = 1.45 \times 10^4$ W m² s kg⁻¹; (a) $\varphi = 0$, (b) $\varphi = 45^\circ$, (c) $\varphi = 90^\circ$, (d) $\varphi = 135^\circ$, (e) $\varphi = 180^\circ$.

5. Results and discussion for a two-frequency resonator

We now extend our considerations to the case where *two* frequencies are present in the resonator so that interference effects can be expected to occur. It will turn out that the nature of the interference depends on whether or not the frequencies are close to each other. We therefore treat the two cases in separate sections.

5.1. Frequencies close to each other

5.1.1. Time history calculations

We assume that the box has different, but very similar, side lengths: $H_x = 1$ m and $H_y = 1.01$ m. The modes (1,0,0) and (0,1,0) therefore have similar frequencies: $\omega_{100} = 1068$ s⁻¹ and $\omega_{010} = 1057$ s⁻¹. The time history of the acoustic velocity was calculated as described in Section 2.4.1, with $\tau = 0.0001$ s and $\varphi = 45^\circ$. The result is shown in Fig. 16(a), and the corresponding frequency spectrum (calculated by FFT) is shown in Fig. 16(b).

For comparison, the equivalent results for a *perfectly square* box ($H_x = H_y = 1$ m) with only one frequency ($\omega_{100} = \omega_{010} = 1068$ s⁻¹) are shown in Figs. 17(a) and (b).

Both cases are damped, but the time histories have very different patterns. The amplitude decreases monotonically in Fig. 17(a). However, in Fig. 16(a), the amplitude shows pronounced fluctuations with successive maxima and minima. This phenomenon is known as "beating". It occurs when two tones with slightly different frequencies are superimposed. The beat frequency is given by the difference between the two constituent frequencies (see e.g. section 89 in [44]). These are represented by the two peaks in the frequency spectrum of Fig. 16(b): $\text{Re}(\Omega_{100}) = 1064.9$ s⁻¹ and $\text{Re}(\Omega_{010}) = 1052.4$ s⁻¹. The beat frequency is therefore $\Delta\Omega = 1064.9$ s⁻¹ - 1052.4 s⁻¹ = 12.5 s⁻¹, and the corresponding beat period is $\frac{2\pi}{\Delta\Omega} = 0.503$ s. This is consistent with Fig. 16(a), where the beats occur approximately every 0.5 s.

The pressure fields corresponding to the results in Figs. 16 and 17 can be seen from Figs. 18 and 19, respectively. These figures show snapshots of the pressure distribution at four different times within one period ($t = 0.1T, 0.25T, 0.5T, 0.75T$) for the nearly square box (Fig. 18) and the perfectly square box (Fig. 19).

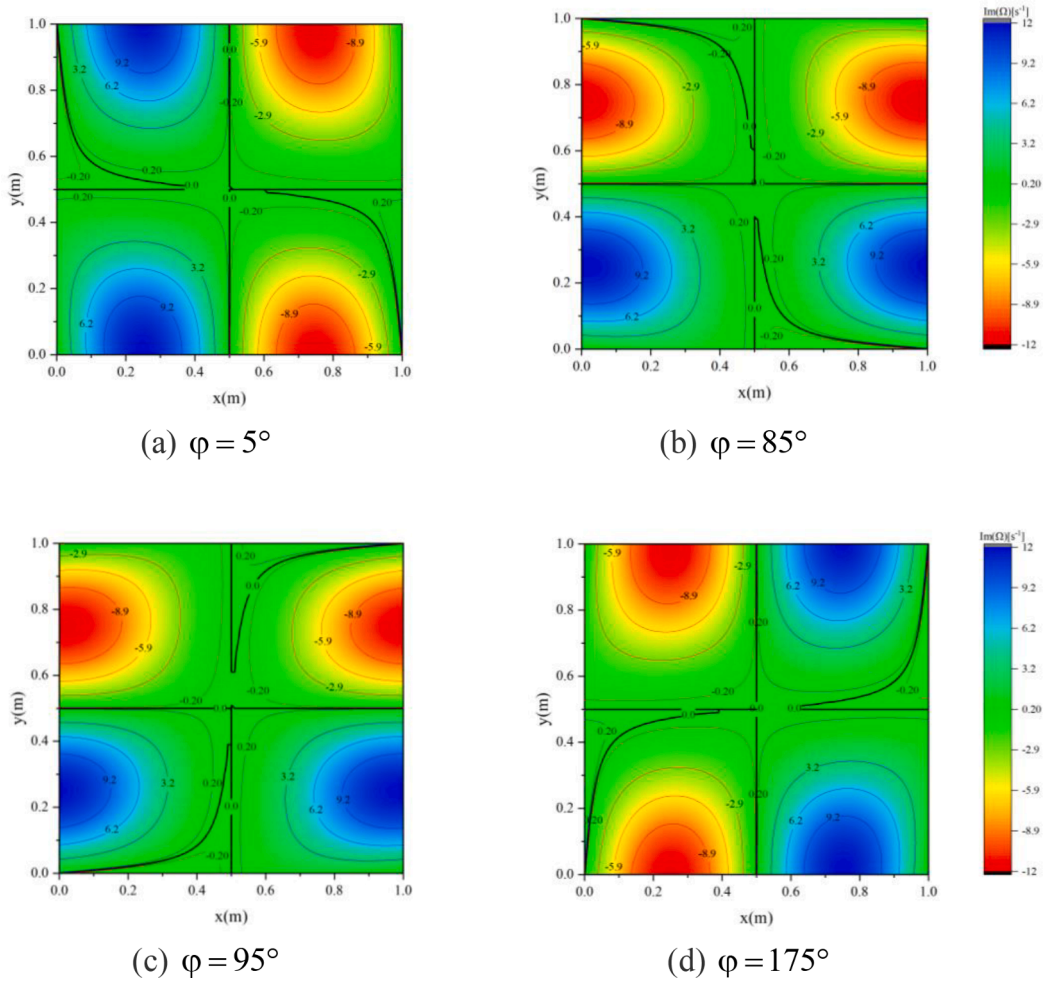


Fig. 15. Contour maps of the growth rate $\text{Im}(\Omega_{110})$ for a square box with side lengths $H_x = H_y = 1$ m, containing a flame with $\tau = 0.001$ s and $K_q n = 1.45 \times 10^4$ W m² s kg⁻¹; (a) $\varphi = 5^\circ$, (b) $\varphi = 85^\circ$, (c) $\varphi = 95^\circ$, (d) $\varphi = 175^\circ$.

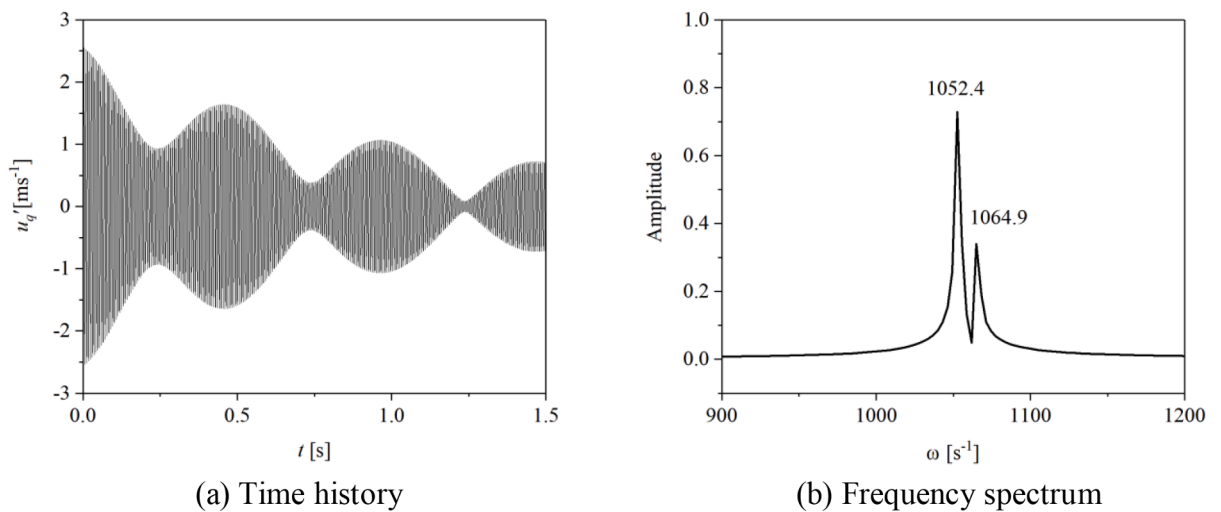


Fig. 16. Acoustic velocity in a *nearly square* box with $H_x = 1$ m, $H_y = 1.01$ m, containing a flame with $x_q = y_q = 0.1$ m, $\varphi = 45^\circ$, $\tau = 0.0001$ s and $K_q n = 1.45 \times 10^4$ W m² s kg⁻¹; (a) time history, (b) frequency spectrum.

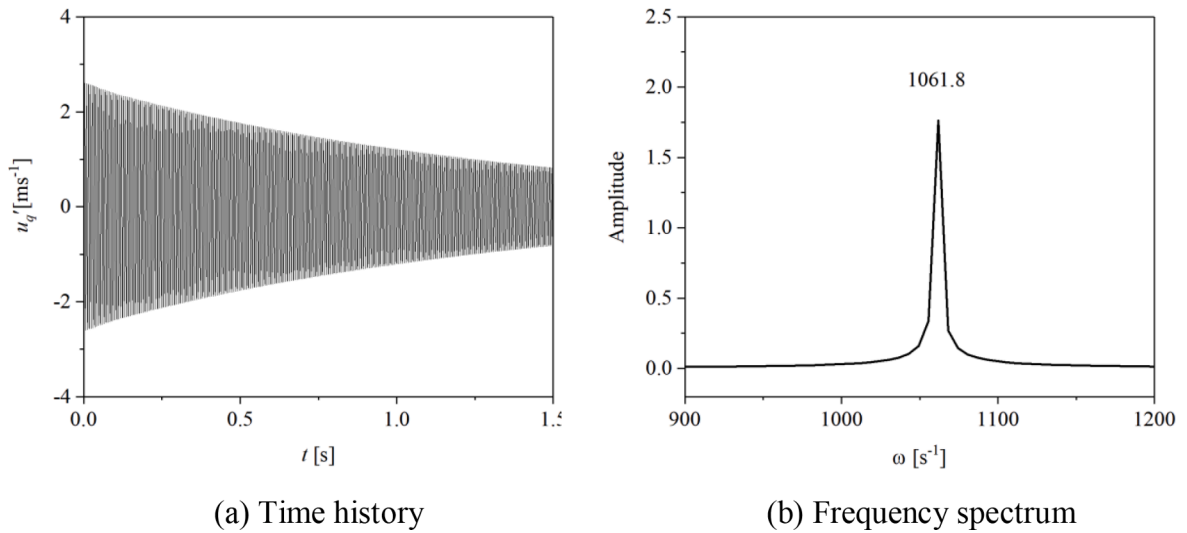


Fig. 17. Acoustic velocity in a perfectly square box with $H_x = H_y = 1$ m, containing a flame with $x_q = y_q = 0.1$ m, $\varphi = 45^\circ$, $\tau = 0.0001$ s and $K_q n = 1.45 \times 10^4$ W m² s kg⁻¹; (a) time history, (b) frequency spectrum.

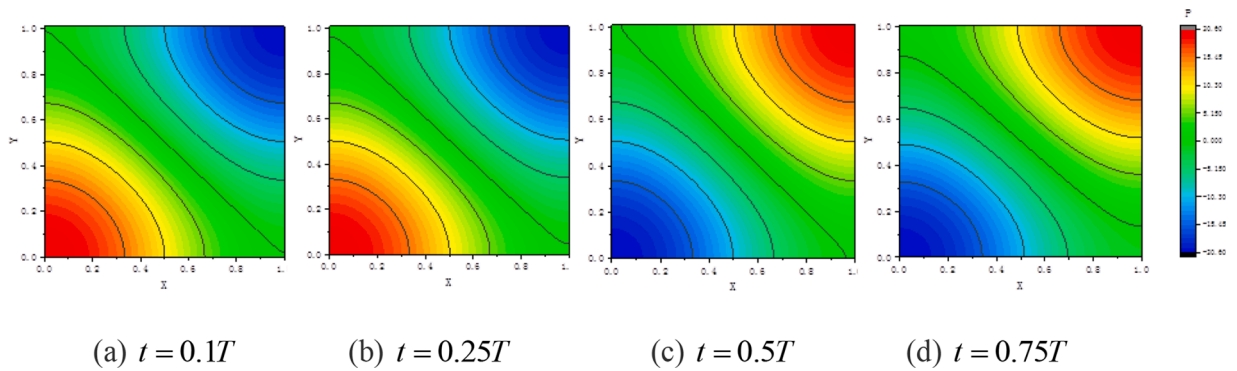


Fig. 18. Acoustic pressure field in a nearly square box at four different times t within one period T . The parameters are the same as for Fig. 16.

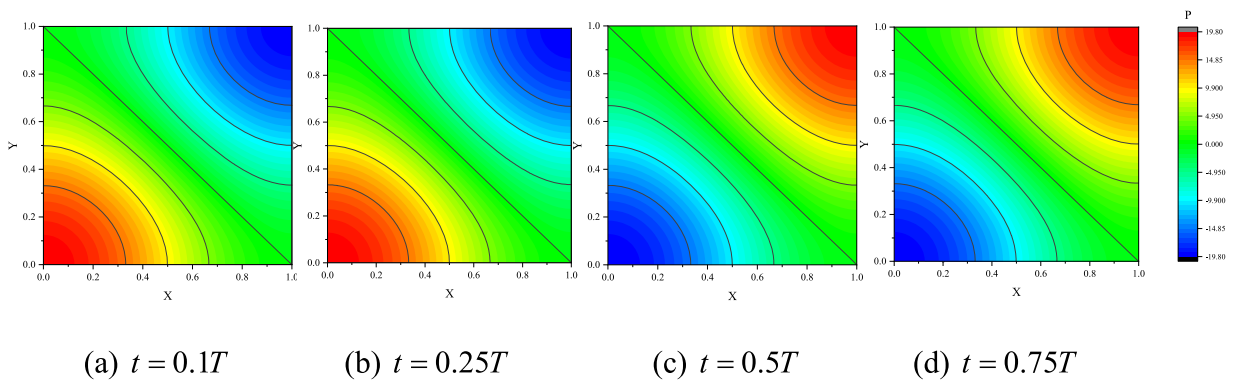


Fig. 19. Acoustic pressure field in a perfectly square box at four different times t within one period T . The parameters are the same as for Fig. 17.

The pressure field in the perfectly square box (Fig. 19) has a nodal line along the diagonal from top left to bottom right, and the pattern is symmetric with respect to the other diagonal. The pressure oscillates in anti-phase on either side of the nodal line. For the nearly square box (Fig. 18), the pattern is very similar except that the "nodal line" is slightly distorted, and the pattern is no longer perfectly symmetric.

5.1.2. Calculation of the thermoacoustic eigenfrequencies

The thermoacoustic eigenfrequencies Ω were calculated as described in Section 2.4.2 for three cases: single mode, degenerate modes, and non-degenerate modes.

Case 1: square box, single mode

The Green's function included the mode (1,0,0); its frequency was $\omega_{100} = 1068 \text{ s}^{-1}$ (for box dimensions $H_x = H_y = 1 \text{ m}$). A single solution, denoted by Ω_{100} , was found for the thermoacoustic eigenfrequency.

Case 2: square box, two degenerate modes

The Green's function included the modes (1,0,0) and (0,1,0); they had the same frequency, $\omega_{100} = \omega_{010} = 1068 \text{ s}^{-1}$ (for box dimensions $H_x = H_y = 1 \text{ m}$). A single solution, denoted by Ω_{100} , was found for the thermoacoustic eigenfrequency.

Case 3: nearly square box, two non-degenerate modes

The Green's function included the modes (1,0,0) and (0,1,0); they had different but similar frequencies, $\omega_{100} = 1068 \text{ s}^{-1}$, $\omega_{010} = 1057 \text{ s}^{-1}$ (for box dimensions $H_x = 1 \text{ m}$, $H_y = 1.01 \text{ m}$). Two solutions, denoted by Ω_{100} and Ω_{010} , were found for the thermoacoustic eigenfrequencies.

Fig. 20 shows the results for all three cases as functions of the time-lag τ ; part (a) of the figure gives the real part (oscillation frequency), and part (b) gives the imaginary part (growth rate) of Ω_{100} , Ω_{010} .

For the square box (cases 1 and 2), the oscillation frequency fluctuates around $\omega_{100} = 1068 \text{ s}^{-1}$ (the eigenfrequency of the box without flame), and the growth rate fluctuates around 0 (the growth rate in the box without flame). The fluctuations are periodic along the τ -axis, with a period of about 0.006 s; this coincides with the period associated with the frequency of 1068 s^{-1} . The same observations were made for the 1-D case [45].

For the nearly square box, there are two thermoacoustic eigenfrequencies, Ω_{100} and Ω_{010} , shown by the blue and green curves in Fig. 20. Their real parts fluctuate in ranges that don't overlap: $\text{Re}(\Omega_{100})$ fluctuates within the range $[1066 \text{ s}^{-1}, 1072 \text{ s}^{-1}]$, while $\text{Re}(\Omega_{010})$ fluctuates within the lower range $[1053 \text{ s}^{-1}, 1059 \text{ s}^{-1}]$. Their imaginary parts are similar, and they have the same signs as those found for cases 1 and 2; however, they are out-of-synch, and this is a manifestation of interference between the two modes.

5.2. Frequencies not close to each other

5.2.1. Time history calculations

We now assume that the box is rectangular with distinctly different side lengths: $H_x = 1 \text{ m}$, $H_y = 1.5 \text{ m}$. The modes (1,0,0) and (0,1,0) then have the frequencies $\omega_{100} = 1068 \text{ s}^{-1}$ and $\omega_{010} = 712 \text{ s}^{-1}$. The time history was again calculated as described in Section 2.4.1, with $\tau = 0.001 \text{ s}$ and $\varphi = 45^\circ$. The result is shown in Fig. 21(a), and the corresponding frequency spectrum (calculated by FFT) is shown in Fig. 21(b).

5.2.2. Calculation of the thermoacoustic eigenfrequencies

The thermoacoustic eigenfrequencies Ω were calculated as described in Section 2.4.2, again for the following three cases: single mode, degenerate modes, and non-degenerate modes.

Case 1: square box, single mode

The Green's function included the mode (1,0,0); its frequency was $\omega_{100} = 712 \text{ s}^{-1}$ (for box dimensions $H_x = H_y = 1.5 \text{ m}$). A single

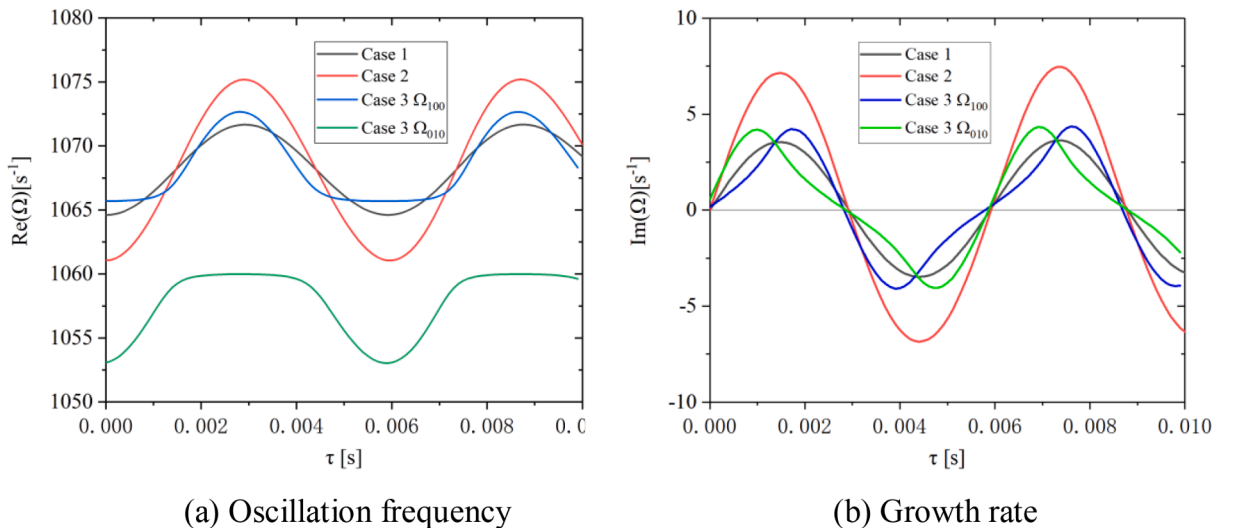
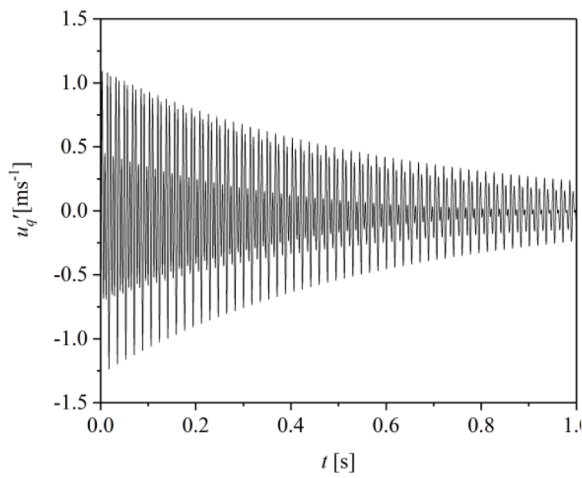
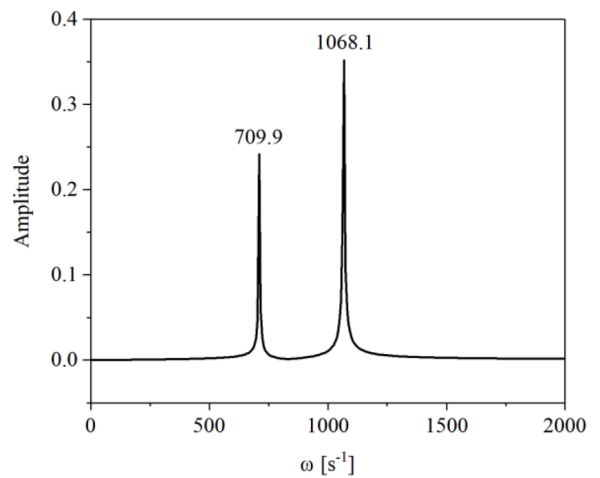


Fig. 20. Complex thermoacoustic eigenfrequencies as functions of the time-lag τ for the three cases listed above with $x_q = y_q = 0.1 \text{ m}$, $\varphi = 45^\circ$, $K_q n = 1.45 \times 10^4 \text{ W m}^2 \text{ s kg}^{-1}$; (a) real part (oscillation frequency), (b) imaginary part (growth rate).

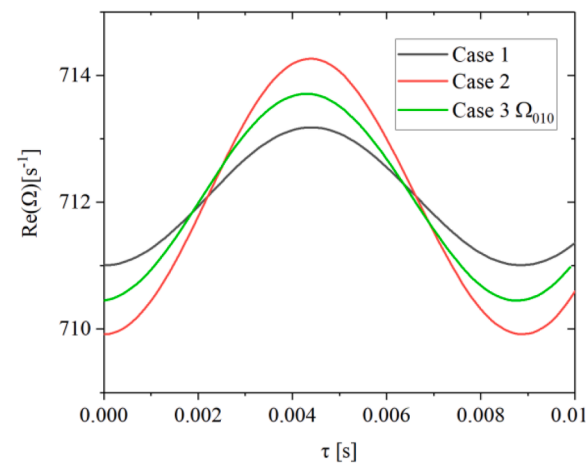
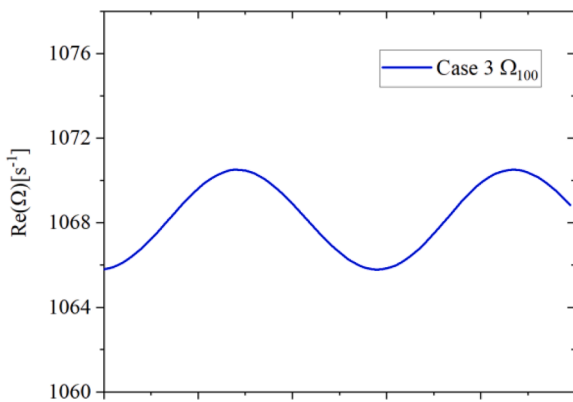


(a) Time history

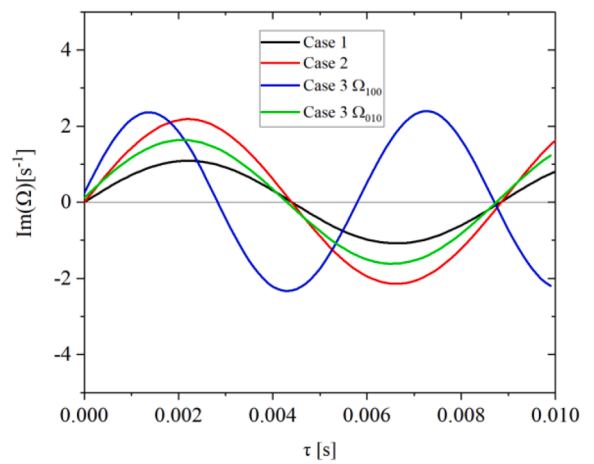


(b) Frequency spectrum

Fig. 21. Acoustic velocity in a box with $H_x = 1$ m, $H_y = 1.5$ m, containing a flame with $x_q = y_q = 0.1$ m, $\varphi = 45^\circ$, $\tau = 0.001$ s and $K_q n = 1.45 \times 10^4$ W m² s kg⁻¹; (a) time history, (b) frequency spectrum.



(a) Oscillation frequency



(b) Growth rate

Fig. 22. Complex thermoacoustic eigenfrequencies as functions of the time-lag τ for the three cases listed above with $x_q = y_q = 0.1$ m, $\varphi = 45^\circ$, $K_q n = 1.45 \times 10^4$ W m² s kg⁻¹; (a) real part (oscillation frequency), (b) imaginary part (growth rate).

solution, denoted by Ω_{100} , was found for the thermoacoustic eigenfrequency.

Case 2: square box, two degenerate modes

The Green's function included the modes (1,0,0) and (0,1,0); they had the same frequency, $\omega_{100} = \omega_{010} = 712 \text{ s}^{-1}$ (for box dimensions $H_x = H_y = 1.5 \text{ m}$). A single solution, denoted by Ω_{100} , was found for the thermoacoustic eigenfrequency.

Case 3: rectangular non-square box, two non-degenerate modes

The Green's function included the modes (1,0,0) and (0,1,0); they had different frequencies, $\omega_{100} = 1068 \text{ s}^{-1}$, $\omega_{010} = 712 \text{ s}^{-1}$ (for box dimensions $H_x = 1 \text{ m}$, $H_y = 1.5 \text{ m}$). Two solutions, denoted by Ω_{100} and Ω_{010} , were found for the thermoacoustic eigenfrequencies.

Fig. 22 shows the results for all three cases as functions of the time-lag τ ; part (a) of the figure gives the real part of Ω_{100} , Ω_{010} (oscillation frequency), and part (b) gives the imaginary part (growth rate).

For the square box (cases 1 and 2), the oscillation frequency fluctuates around $\omega_{100} = 712 \text{ s}^{-1}$ (the eigenfrequency of the box without flame), and the growth rate fluctuates around 0 (the growth rate in the box without flame). The fluctuations are periodic along the τ -axis, with a period of about 0.009 s; this coincides with the period associated with the frequency of 712 s^{-1} .

For the non-square box, there are two thermoacoustic eigenfrequencies, Ω_{100} and Ω_{010} , shown by the blue and green curves in Fig. 22. Their real parts are distinctly different: $\text{Re}(\Omega_{100})$ fluctuates within the range $[1065 \text{ s}^{-1}, 1070 \text{ s}^{-1}]$, while $\text{Re}(\Omega_{010})$ fluctuates within the lower range $[710.3 \text{ s}^{-1}, 713.2 \text{ s}^{-1}]$. Their imaginary parts fluctuate in the ranges $[-2.4 \text{ s}^{-1}, +2.4 \text{ s}^{-1}]$ for $\text{Im}(\Omega_{100})$, and $[-1.7 \text{ s}^{-1}, +1.7 \text{ s}^{-1}]$ for $\text{Im}(\Omega_{010})$.

5.3. Results and discussion for a three-frequency resonator

We briefly consider a three-mode interference in a rectangular box with side lengths $H_x = 1 \text{ m}$, $H_y = 2 \text{ m}$. The following three modes were included in the Green's function: (1,0,0), (0,1,0) and (1,1,0). Their individual frequencies are: $\omega_{100} = 1068 \text{ s}^{-1}$, $\omega_{010} = 534 \text{ s}^{-1}$ and $\omega_{110} = 1194 \text{ s}^{-1}$. The time history was again calculated as described in Section 2.4.1, with $\tau = 0.001 \text{ s}$ and $\varphi = 45^\circ$. The result is shown in Fig. 23(a), and the corresponding frequency spectrum (calculated by FFT) is shown in Fig. 23(b).

The frequency spectrum has peaks at the frequencies 534.1 Hz, 1068.1 Hz and 1193.4 Hz, which are very similar to the eigenfrequencies of the Green's function modes. The last two peaks have similar frequencies and relatively large amplitudes, and they are responsible for the beating that can be seen in the time history.

The acoustic field resulting from the superposition of these three thermoacoustic modes is visualised in Fig. 24. Snapshots are shown at four different times, $t = 0.1T$, $0.25T$, $0.5T$, $0.75T$, where T is the oscillation period of the (0,1,0) mode.

The pressure distribution undergoes irregular changes with time; nodal lines or nodal curves are absent.

6. Conclusions and outlook

This paper presents a 3-D analytical model, based on a Green's function approach, of a compact flame in a hard-walled rectangular cavity. The heat release rate from the flame is described by a time-lag law, which takes into account the direction of the flame. The cavity is described by its tailored Green's function. The complete system is modelled by an integral equation for the acoustic velocity at the flame position. Stability predictions are made from this integral equation in two ways:

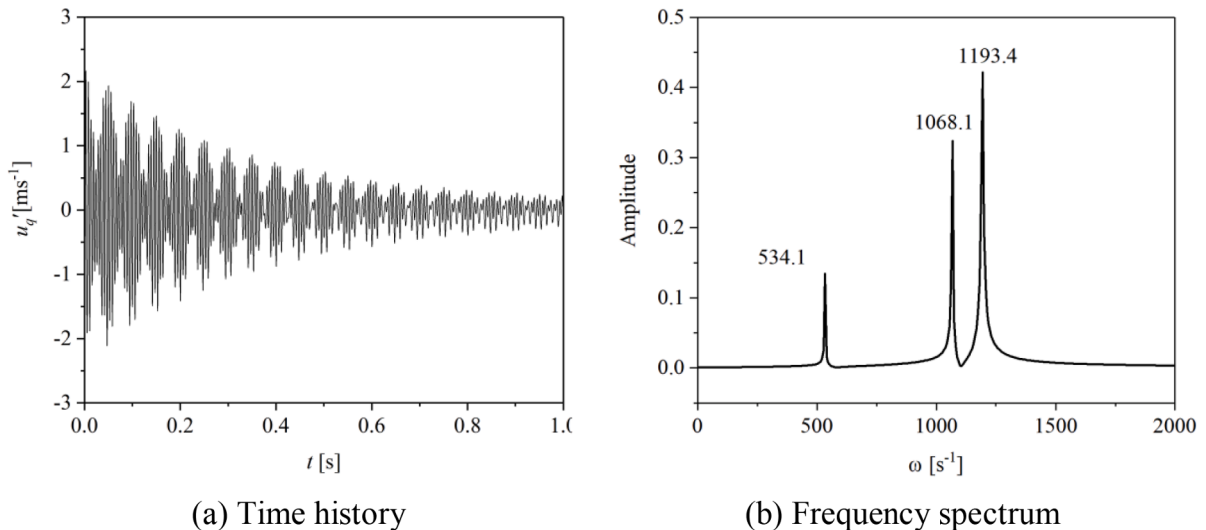


Fig. 23. Acoustic velocity in a box with $H_x = 1 \text{ m}$, $H_y = 2 \text{ m}$, containing a flame with $x_q = y_q = 0.1 \text{ m}$, $\varphi = 45^\circ$, $\tau = 0.001 \text{ s}$ and $K_q n = 1.45 \times 10^4 \text{ W m}^2 \text{ s kg}^{-1}$; (a) time history, (b) frequency spectrum.

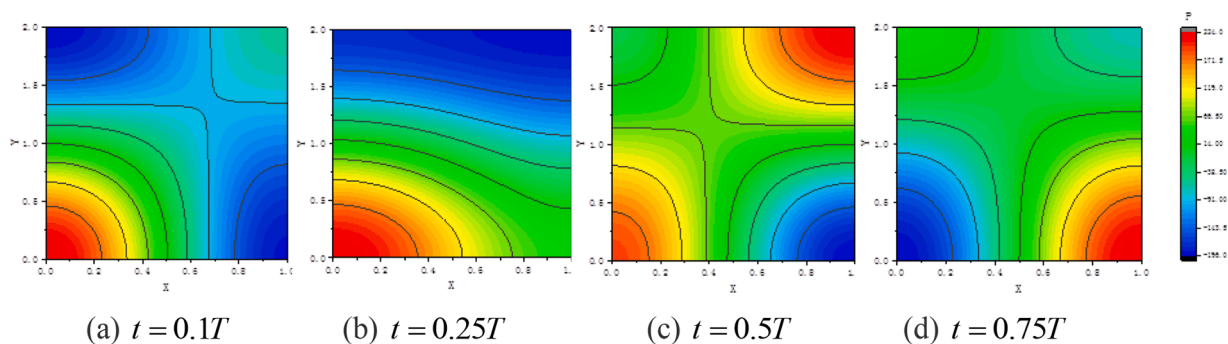


Fig. 24. Snapshots at four different times t of the acoustic pressure in the box with modes (1,0,0), (0,1,0) and (1,1,0) superimposed. The parameters are the same as in Fig. 23.

- by solving it directly with a numerical time stepping approach to obtain the time history of the acoustic velocity;
- by deriving from it a nonlinear algebraic equation for the complex thermoacoustic eigenfrequencies.

A range of parametric studies revealed some new phenomena, which cannot occur in a 1-D situation:

- (1) Inside the cavity, there is a 3-D standing wave field with a spatial distribution of the acoustic pressure and velocity; the position of the compact flame within this 3-D standing wave field is crucial for the stability behaviour.
- (2) The flame direction, described by the angle φ , affects the stability behaviour; careful choice of φ can make a previously unstable system stable.
- (3) Modes with similar frequencies can coexist in a 3-D cavity. The interference of such modes leads to the well-known beat effect, i. e. a periodic increase and decrease of the oscillation amplitude.

Our study could be extended in several ways:

- (1) More complex (and even nonlinear) flame models can be incorporated, as long as the flame is compact and its local heat release rate is known as a function of the velocity perturbation at the flame. For example, one could obtain a flame transfer function from CFD simulations or measurement, and then transform it from the frequency-domain to the time-domain; there are physically inspired analytical tools to execute such a transform [46,47] with very little numerical effort.
- (2) In this study we have included a *single* flame in our model. This can be extended to include several flames, as long as they can be regarded as compact. In fact, our Green's function approach is ideally suited for this purpose.
- (3) The assumption of a *uniform* temperature field could be relaxed. This would require the calculation of a more elaborate tailored Green's function, which could be done by dividing the cavity volume into segments, each with its own uniform temperature, to approximate a given temperature distribution.
- (4) Since the tailored Green's function is known not just for rectangular cavities, but also for cylindrical cavities, our method can be applied to annular combustion chambers.

CRediT authorship contribution statement

Xiaoyu Wang: Conceptualization, Methodology, Software, Validation, Formal analysis, Investigation, Data curation, Writing – original draft, Visualization, Funding acquisition. **Maria Heckl:** Conceptualization, Methodology, Formal analysis, Investigation, Resources, Writing – review & editing, Visualization, Supervision, Project administration.

Declaration of Competing Interest

The authors declare that they have no known competing financial interests or personal relationships that could have appeared to influence the work reported in this paper.

Acknowledgements

The authors gratefully acknowledge the financial support from the National Natural Science Foundation of China (grant numbers: 51676008 and 51790514).

Appendix A. – Derivation of the tailored Green's function for a 3-D hard-walled rectangular resonator

The governing equations for the tailored Green's function, $G(\vec{r}, \vec{r}', t - t')$, are the nonhomogeneous wave Eq. (1) and the hard-wall boundary conditions (zero normal derivative at each cavity wall). For convenience, these equations are written here in terms of the source coordinates \vec{r}' and t' ,

$$\frac{1}{c^2} \frac{\partial^2 G}{\partial t'^2} - \frac{\partial^2 G}{\partial \vec{r}'^2} = \delta(\vec{r} - \vec{r}') \delta(t - t') \quad (\text{A1})$$

and

$$\left. \frac{\partial G}{\partial \vec{r}'} \right|_{\text{cavity wall}} = 0. \quad (\text{A2})$$

Eq. (A1) can be Fourier-transformed into the frequency-domain. To this end, we introduce the Fourier transform pair

$$\widehat{G}(\vec{r}, \vec{r}', \omega) = \int_{-\infty}^{\infty} G(\vec{r}, \vec{r}', t - t') e^{j\omega(t-t')} dt', \quad (\text{A3a})$$

$$G(\vec{r}, \vec{r}', t - t') = \frac{1}{2\pi} \int_{-\infty}^{\infty} \widehat{G}(\vec{r}, \vec{r}', \omega) e^{-j\omega(t-t')} d\omega. \quad (\text{A3b})$$

The frequency-domain version of (A1) is

$$\frac{\partial^2 \widehat{G}}{\partial \vec{r}'^2} + k_0^2 \widehat{G} = -\delta(\vec{r} - \vec{r}'), \quad (\text{A4})$$

where

$$k_0 = \frac{\omega^2}{c^2}. \quad (\text{A5})$$

The boundary conditions (A2) retain their form in the frequency domain,

$$\left. \frac{\partial \widehat{G}}{\partial \vec{r}'} \right|_{\text{cavity wall}} = 0. \quad (\text{A6})$$

In order to satisfy the boundary conditions, we assume a trial solution for \widehat{G} , which is a superposition of the eigenfunctions $\psi_{mnk}(\vec{r}')$,

$$\widehat{G}(\vec{r}, \vec{r}', \omega) = \sum_{\substack{m,n,k=0 \\ (m,n,k) \neq (0,0,0)}}^{\infty} A_{mnk} \psi_{mnk}(\vec{r}'), \quad (\text{A7})$$

with unknown coefficients A_{mnk} . The eigenfunctions satisfy the Helmholtz equation,

$$\frac{\partial^2 \psi_{mnk}(\vec{r}')}{\partial \vec{r}'^2} + k_{mnk}^2 \psi_{mnk}(\vec{r}') = 0, \quad (\text{A8})$$

and are given by

$$\psi_{mnk}(\vec{r}') = \cos(k_x x') \cos(k_y y') \cos(k_z z'), \quad (\text{A9})$$

with

$$k_x = \frac{m\pi}{H_x}, \quad k_y = \frac{n\pi}{H_y}, \quad k_z = \frac{k\pi}{H_z}, \quad (\text{A10})$$

and

$$k_{mnk} = \sqrt{k_x^2 + k_y^2 + k_z^2}. \quad (\text{A11})$$

In order to determine the coefficients A_{mnk} , we perform the following series of mathematical steps. First, we substitute (A7) into the PDE (A4) for the Green's function,

$$\sum_{m,n,k=0}^{\infty} A_{mnk} \left[\frac{\partial^2 \psi_{mnk}}{\partial \vec{r}'^2} + k_0^2 \psi_{mnk}(\vec{r}') \right] = -\delta(\vec{r} - \vec{r}'). \tag{A12}$$

Next, we substitute for $\frac{\partial^2 \psi_{mnk}}{\partial \vec{r}'^2}$ with (A8),

$$\sum_{m,n,k=0}^{\infty} A_{mnk} (-k_{mnk}^2 + k_0^2) \psi_{mnk}(\vec{r}') = -\delta(\vec{r} - \vec{r}'). \tag{A13}$$

Then we multiply (A13) by $\psi_{m'n'k'}(\vec{r}')$ (eigenfunction corresponding to mode $(m'n'k')$) and integrate over the volume of the cavity,

$$\sum_{m,n,k=0}^{\infty} A_{mnk} (k_0^2 - k_{mnk}^2) \int_{\text{cavity}} \psi_{mnk}(\vec{r}') \psi_{m'n'k'}(\vec{r}') d^3 r' = -\psi_{m'n'k'}(\vec{r}'). \tag{A14}$$

Due to the orthogonality of the eigenfunctions, the integrals over the cavity volume are zero if $(m,n,k) \neq (m',n',k')$. The remaining non-zero integrals can be calculated directly from (A9), and the result is

$$\int_{\text{cavity}} [\psi_{mnk}(\vec{r}')]^2 d^3 r' = \frac{\Gamma_{mnk}}{\varepsilon_m \varepsilon_n \varepsilon_k}, \tag{A15}$$

where

$$\Gamma_{mnk} = H_x H_y H_z, \tag{A16}$$

$$\varepsilon_m = \begin{cases} 1 & \text{if } m = 0 \\ 2 & \text{if } m > 0 \end{cases} \text{ (same for } \varepsilon_n \text{ and } \varepsilon_k). \tag{A17}$$

Eq. (A14) can then be written without the sum and solved for A_{mnk} ; this leads to

$$A_{mnk} = -\psi_{mnk}(\vec{r}') \frac{\varepsilon_m \varepsilon_n \varepsilon_k}{(k_0^2 - k_{mnk}^2) \Gamma_{mnk}}. \tag{A18}$$

Substitution of this into (A7) gives the final result for the Green's function in the frequency-domain,

$$\widehat{G}(\vec{r}, \vec{r}', \omega) = - \sum_{\substack{m,n,k=0 \\ (m,n,k) \neq (0,0,0)}}^{\infty} \frac{\varepsilon_m \varepsilon_n \varepsilon_k}{(k_0^2 - k_{mnk}^2) \Gamma_{mnk}} \psi_{mnk}(\vec{r}') \psi_{mnk}(\vec{r}). \tag{A19}$$

By applying the inverse Fourier transform (A3b) to (A19), the Green's function in the time-domain is obtained,

$$G(\vec{r}, \vec{r}', t - t') = - \frac{1}{2\pi} \sum_{\substack{m,n,k=0 \\ (m,n,k) \neq (0,0,0)}}^{\infty} \frac{\varepsilon_m \varepsilon_n \varepsilon_k}{\Gamma_{mnk}} \psi_{mnk}(\vec{r}') \psi_{mnk}(\vec{r}) \int_{-\infty}^{\infty} \frac{e^{j\omega(t-t')}}{k_0^2 - k_{mnk}^2} d\omega. \tag{A20}$$

Appendix B. Derivation of the iteration scheme in Section 2.4.1

The starting point of this derivation is the integral Eq. (19)

$$u(t) = \int_{t'=0}^t K(t, t') u(t' - \tau) dt' + f(t). \tag{B1}$$

The presence of the time-lag τ makes it necessary to supplement the initial conditions (17) by additional conditions specified for earlier times $t < 0$. We impose

$$u(t' - \tau) = 0 \text{ for } t' \leq \tau. \tag{B2}$$

The lower integration limit in (B1) can then be replaced by τ . After discretisation of t by

$$t_N = Nh, \quad (\text{B3})$$

Eq. (B1) can be written as

$$u(t_N) = \int_{t'=\tau}^{t_N} K(t_N, t')u(t' - \tau) dt' + f(t_N). \quad (\text{B4})$$

The time-lag is discretised by

$$\tau = Mh, \quad M = 1, 2, 3, \dots \quad (\text{B5})$$

where M is fixed – in contrast to N , which increases with each iteration step. The discretised form of the time interval $t' - \tau$ is then t_{N-M} . By applying the trapezoidal rule to the integral in (B4), we get

$$u(t_N) = \frac{h}{2} \sum_{i=M+1}^N [K(t_N, t_{i-1})u(t_{i-M-1}) + K(t_N, t_i)u(t_{i-M})] + f(t_N). \quad (\text{B6})$$

A more convenient form of (B6) is obtained by rearranging the terms of the sum:

$$u(t_N) = f(t_N) + \frac{h}{2} [K(t_N, t_M)u(t_0) + K(t_N, t_N)u(t_{N-M})] + h \sum_{i=M}^{N-2} K(t_N, t_{i+1})u(t_{i-M+1}). \quad (\text{B7})$$

For the first few iteration steps, all u -terms on the right hand side are zero, which leaves

$$N = 0 : u(t_0) = f(t_0) \quad (\text{B8a})$$

$$N = 1 : u(t_1) = f(t_1) \quad (\text{B8b})$$

⋮

$$N = M : u(t_M) = f(t_M) \quad (\text{B8c})$$

For the next two iteration steps, we get

$$N = M + 1 : u(t_{M+1}) = f(t_{M+1}) + \frac{h}{2} [K(t_{M+1}, t_M)u(t_0) + K(t_{M+1}, t_{M+1})u(t_1)] \quad (\text{B8d})$$

$$N = M + 2 : u(t_{M+2}) = f(t_{M+2}) + \frac{h}{2} [K(t_{M+2}, t_M)u(t_0) + K(t_{M+2}, t_{M+2})u(t_2)] + hK(t_{M+2}, t_{M+1})u(t_1) \quad (\text{B8e})$$

All subsequent iteration steps are performed with (B7).

Appendix C. Derivation of the equations for $\Omega_{\mu\nu\kappa}$ and $u_{\mu\nu\kappa}$ in Section 2.4.2

The starting point of this derivation is the governing Eq. (19) for the velocity fluctuation $u'_q(t)$,

$$u'_q(t) = -\frac{\gamma-1}{c^2} K_q n \int_0^t \left(\frac{\partial G(\vec{r}, \vec{r}', t-t')}{\partial r} \right) \Bigg|_{\substack{\vec{r}' = \vec{r}_q \\ \vec{r} = \vec{r}_q}} u'_q(t' - \tau) dt' - \frac{\phi_0}{c^2} \left(\frac{\partial^2 G}{\partial r \partial t'} \right) \Bigg|_{\substack{t' = 0 \\ \vec{r}' = \vec{r}_q \\ \vec{r} = \vec{r}_q}}. \quad (\text{C1})$$

The derivatives of the Green's function that occur in (C1) are obtained from (11),

$$\left(\frac{\partial G(\vec{r}, \vec{r}', t-t')}{\partial r} \right) \Bigg|_{\substack{\vec{r}' = \vec{r}_q \\ \vec{r} = \vec{r}_q}} = \sum_{mnk} G_{mnk} \frac{1}{2} [e^{j\omega_{mnk}(t-t')} - e^{-j\omega_{mnk}(t-t')}], \quad (\text{C2})$$

$$\left(\frac{\partial^2 G}{\partial r \partial t'} \right) \Bigg|_{\substack{t' = 0 \\ \vec{r}' = \vec{r}_q \\ \vec{r} = \vec{r}_q}} = \sum_{mnk} G_{mnk} \frac{1}{2} j\omega_{mnk} (-e^{j\omega_{mnk}t} - e^{-j\omega_{mnk}t}), \quad (\text{C3})$$

with the abbreviation

$$G_{mnk} = \left. \frac{\partial g_{mnk}(\vec{r}, \vec{r}')}{\partial r} \right|_{\substack{\vec{r}' = \vec{r}_q \\ \vec{r} = \vec{r}_q}} \quad (C4)$$

The trial solution for $u'_q(t)$ is given by (29), and its time-lagged version is

$$u'_q(t - \tau) = \sum_{\mu\nu\kappa} u_{\mu\nu\kappa} e^{i\Omega_{\mu\nu\kappa}(t - \tau)}. \quad (C5)$$

After substitution with (C2), (C3) and (C5), the governing Eq. (C1) becomes

$$\begin{aligned} \sum_{\mu\nu\kappa} u_{\mu\nu\kappa} e^{i\Omega_{\mu\nu\kappa}t} = & -\frac{\gamma-1}{c^2} K_q n \int_0^t \sum_{mnk} G_{mnk} \frac{1}{2} [e^{i\omega_{mnk}(t-t')} - e^{-j\omega_{mnk}(t-t')}] \sum_{\mu\nu\kappa} u_{\mu\nu\kappa} e^{i\Omega_{\mu\nu\kappa}(t'-\tau)} dt' - \\ & - \frac{\phi_0}{c^2} \sum_{mnk} G_{mnk} \frac{1}{2} j\omega_{mnk} (-e^{j\omega_{mnk}t} - e^{-j\omega_{mnk}t}). \end{aligned} \quad (C6)$$

We rearrange the terms on the right hand side by putting the terms independent of t' outside the integral,

$$\begin{aligned} \sum_{\mu\nu\kappa} u_{\mu\nu\kappa} e^{i\Omega_{\mu\nu\kappa}t} = & -\frac{\gamma-1}{c^2} K_q n \sum_{mnk} \sum_{\mu\nu\kappa} \frac{1}{2} G_{mnk} u_{\mu\nu\kappa} e^{-j\Omega_{\mu\nu\kappa}\tau} \left\{ e^{i\omega_{mnk}t} \int_0^t [e^{j(-\omega_{mnk} + \Omega_{\mu\nu\kappa})t'} dt' - \right. \\ & \left. - e^{-j\omega_{mnk}t} \int_0^t e^{j(\omega_{mnk} + \Omega_{\mu\nu\kappa})t'} dt' \right\} + \\ & + \frac{\phi_0}{c^2} \sum_{mnk} \frac{1}{2} G_{mnk} j\omega_{mnk} (e^{j\omega_{mnk}t} + e^{-j\omega_{mnk}t}). \end{aligned} \quad (C7)$$

The integrals with respect to t' can be evaluated,

$$\int_0^t e^{j(\pm\omega_{mnk} + \Omega_{\mu\nu\kappa})t'} dt' = \frac{e^{j(\pm\omega_{mnk} + \Omega_{\mu\nu\kappa})t} - 1}{j(\pm\omega_{mnk} + \Omega_{\mu\nu\kappa})}. \quad (C8)$$

With this, (C7) can be written as

$$\begin{aligned} \sum_{\mu\nu\kappa} u_{\mu\nu\kappa} e^{i\Omega_{\mu\nu\kappa}t} = & -\frac{\gamma-1}{c^2} K_q n \sum_{mnk} \sum_{\mu\nu\kappa} \frac{1}{2} G_{mnk} u_{\mu\nu\kappa} e^{-j\Omega_{\mu\nu\kappa}\tau} \left[\frac{e^{j\Omega_{\mu\nu\kappa}t} - e^{j\omega_{mnk}t}}{j(-\omega_{mnk} + \Omega_{\mu\nu\kappa})} - \frac{e^{j\Omega_{\mu\nu\kappa}t} - e^{-j\omega_{mnk}t}}{j(\omega_{mnk} + \Omega_{\mu\nu\kappa})} \right] + \\ & + \frac{\phi_0}{c^2} \sum_{mnk} \frac{1}{2} G_{mnk} j\omega_{mnk} (e^{j\omega_{mnk}t} + e^{-j\omega_{mnk}t}). \end{aligned} \quad (C9)$$

In the next step, we group the terms with factors $u_{\mu\nu\kappa} e^{i\Omega_{\mu\nu\kappa}t}$, $G_{mnk} e^{j\omega_{mnk}t}$, $G_{mnk} e^{-j\omega_{mnk}t}$:

$$\begin{aligned} \sum_{\mu\nu\kappa} u_{\mu\nu\kappa} e^{i\Omega_{\mu\nu\kappa}t} = & -\frac{\gamma-1}{c^2} K_q n \left\{ \sum_{\mu\nu\kappa} u_{\mu\nu\kappa} e^{i\Omega_{\mu\nu\kappa}t} e^{-j\Omega_{\mu\nu\kappa}\tau} \sum_{mnk} \frac{1}{2} G_{mnk} \left[\frac{1}{j(-\omega_{mnk} + \Omega_{\mu\nu\kappa})} - \frac{1}{j(\omega_{mnk} + \Omega_{\mu\nu\kappa})} \right] - \right. \\ & \left. - \sum_{mnk} \frac{1}{2} G_{mnk} e^{j\omega_{mnk}t} \sum_{\mu\nu\kappa} \frac{u_{\mu\nu\kappa} e^{-j\Omega_{\mu\nu\kappa}\tau}}{j(-\omega_{mnk} + \Omega_{\mu\nu\kappa})} + \sum_{mnk} \frac{1}{2} G_{mnk} e^{-j\omega_{mnk}t} \sum_{\mu\nu\kappa} \frac{u_{\mu\nu\kappa} e^{-j\Omega_{\mu\nu\kappa}\tau}}{j(\omega_{mnk} + \Omega_{\mu\nu\kappa})} \right\} + \\ & + \sum_{mnk} \frac{1}{2} G_{mnk} e^{j\omega_{mnk}t} \frac{\phi_0}{c^2} j\omega_{mnk} + \sum_{mnk} \frac{1}{2} G_{mnk} e^{-j\omega_{mnk}t} \frac{\phi_0}{c^2} j\omega_{mnk}. \end{aligned} \quad (C10)$$

This equation is satisfied if the coefficients of $u_{\mu\nu\kappa}e^{j\Omega_{\mu\nu\kappa}t}$, $G_{mnk}e^{j\omega_{mnk}t}$ and $G_{mnk}e^{-j\omega_{mnk}t}$ are equal on either side of the equation. Equating the coefficients of $u_{\mu\nu\kappa}e^{-j\Omega_{\mu\nu\kappa}t}$ gives

$$1 = -\frac{\gamma-1}{c^2}K_q n e^{-j\Omega_{\mu\nu\kappa}t} \sum_{mnk} \frac{1}{2} G_{mnk} \left[\frac{1}{j(-\omega_{mnk} + \Omega_{\mu\nu\kappa})} - \frac{1}{j(\omega_{mnk} + \Omega_{\mu\nu\kappa})} \right]. \quad (C11)$$

This is a nonlinear equation for the heat-driven frequencies $\Omega_{\mu\nu\kappa}$. It has infinitely many solutions, each solution corresponding to a particular thermoacoustic mode. Equating the coefficients of $G_{mnk}e^{j\omega_{mnk}t}$ leads to

$$-\frac{\gamma-1}{c^2}K_q n \sum_{\mu\nu\kappa} \frac{e^{-j\Omega_{\mu\nu\kappa}t}}{j(-\omega_{mnk} + \Omega_{\mu\nu\kappa})} u_{\mu\nu\kappa} = \frac{\phi_0}{c^2} j\omega_{mnk}. \quad (C12)$$

This is a linear set of equations for the amplitudes $u_{\mu\nu\kappa}$. An equivalent equation, i.e. no new information, is obtained by equating the coefficients of $G_{mnk}e^{-j\omega_{mnk}t}$.

References

- [1] S. Candel, Combustion dynamics and control: Progress and challenges, *Proc. Combust. Inst.* 29 (2002) 1–28, [https://doi.org/10.1016/S1540-7489\(02\)80007-4](https://doi.org/10.1016/S1540-7489(02)80007-4).
- [2] T. Lieuwen, Modeling premixed combustion-acoustic wave interactions: A review, *J. Propuls. Power* 19 (2003) 765–781, <https://doi.org/10.2514/2.6193>.
- [3] Y. Huang, V. Yang, Dynamics and stability of lean-premixed swirl-stabilized combustion, *Prog. Energy Combust. Sci.* 35 (2009) 293–364, <https://doi.org/10.1016/j.pecs.2009.01.002>.
- [4] T.C. Lieuwen, V. Yang, *Combustion Instabilities in Gas Turbine Engines*, American Institute of Aeronautics and Astronautics, 2005.
- [5] T. Poinso, D. Veynante, *Theoretical and Numerical Combustion*, 2nd edition, Edwards, Philadelphia, 2005.
- [6] Culick, F.E.C. (2006) *Unsteady motions in combustion chambers for propulsion systems*. Research and Technology Organisation, NATO, RTO-AG-AVT-039.
- [7] W. Lang, T. Poinso, S. Candel, Active control of combustion instability, *Combust. Flame* 70 (1987) 281–289, [https://doi.org/10.1016/0010-2180\(87\)90109-X](https://doi.org/10.1016/0010-2180(87)90109-X).
- [8] T.J. Poinso, A.C. Trouve, D.P. Veynante, S.M. Candel, E.J. Esposito, Vortex-driven acoustically coupled combustion instabilities, *J. Fluid Mech.* 177 (1987) 265–292, <https://doi.org/10.1017/S0022112087000958>.
- [9] G.J. Bloxidge, A.P. Dowling, P.J. Langhorne, Reheat buzz - an acoustically coupled combustion instability. Part 2. Theory, *J. Fluid Mech.* 193 (1988) 445–473, <https://doi.org/10.1017/S0022112088002216>.
- [10] M.A. Heckl, Active control of the noise from a Rijke tube, *J. Sound Vib.* 124 (1988) 117–133, [https://doi.org/10.1016/S0022-460X\(88\)81408-1](https://doi.org/10.1016/S0022-460X(88)81408-1).
- [11] M.A. Heckl, Non-linear acoustic effects in the Rijke tube, *Acustica* 72 (1990) 63–71.
- [12] N. Noiray, D. Durox, T. Schuller, S. Candel, Self-induced instabilities of premixed flames in a multiple injection configuration, *Combust. Flame* 145 (2006) 435–446, <https://doi.org/10.1016/j.combustflame.2006.01.006>.
- [13] S. Mariappan, R.I. Sujith, Modelling nonlinear thermoacoustic instability in an electrically heated Rijke tube, *J. Fluid Mech.* 680 (2011) 511–533, <https://doi.org/10.1017/jfm.2011.176>.
- [14] E.A. Gopalakrishnan, R.I. Sujith, Effect of external noise on the hysteresis characteristics of a thermoacoustic system, *J. Fluid Mech.* 776 (2015) 334–353, <https://doi.org/10.1017/jfm.2015.330>.
- [15] B. Mohan, S. Mariappan, Nonlinear stability analysis of intrinsic thermoacoustic modes in a one-dimensional longitudinal combustor, *Combust. Flame* 215 (2020) 309–323, <https://doi.org/10.1016/j.combustflame.2020.02.011>.
- [16] J. Li, Y. Xia, A.S. Morgans, X. Han, Numerical prediction of combustion instability limit cycle oscillations for a combustor with a long flame, *Combust. Flame* 185 (2017) 28–43, <https://doi.org/10.1016/j.combustflame.2017.06.018>.
- [17] N. Noiray, M. Bothien, B. Schuermans, Investigation of azimuthal staging concepts in annular gas turbines, *Combust. Theory Model.* 15 (2011) 585–606, <https://doi.org/10.1080/13647830.2011.552636>.
- [18] J.-F. Parmentier, P. Salas, P. Wolf, G. Staffelbach, F. Nicoud, T. Poinso, A simple analytical model to study and control azimuthal instabilities in annular combustion chambers, *Combust. Flame* 159 (2012) 2374–2387, <https://doi.org/10.1016/j.combustflame.2012.02.007>.
- [19] G. Ghirardo, M.P. Juniper, Azimuthal instabilities in annular combustors: standing and spinning modes, *Proc. R. Soc. Lond. A* 469 (2013), <https://doi.org/10.1098/rspa.2013.0232> paper 20130232.
- [20] M. Bauerheim, J.-F. Parmentier, P. Salas, F. Nicoud, T. Poinso, An analytical model for azimuthal thermoacoustic modes in an annular chamber fed by an annular plenum, *Combust. Flame* 161 (2014) 1374–1389, <https://doi.org/10.1016/j.combustflame.2013.11.014>.
- [21] S.R. Stow, A.P. Dowling, Thermoacoustic oscillations in an annular combustor, in: *Proceedings of the ASME Turbo Expo 2001, New Orleans, Louisiana, USA, 4-7 June 2001*, 2001, pp. 1–8.
- [22] S. Evesque, W. Polifke, Low-order acoustic modelling for annular combustors: validation and inclusion of modal coupling, in: *Proceedings of the ASME Turbo Expo 2002, Amsterdam, The Netherlands, 3-6 June 2002*, 2002 paper no GT-2002-30064.
- [23] L. Li, X. Sun, Effect of vorticity waves on azimuthal instabilities in annular chambers, *Combust. Flame* 162 (2015) 628–641, <https://doi.org/10.1016/j.combustflame.2014.09.011>.
- [24] F. Nicoud, L. Benoit, C. Sensiau, T. Poinso, Acoustic modes in combustors with complex impedances and multidimensional active flames, *AIAA Journal* 45 (2007) 426–441, <https://doi.org/10.2514/1.24933>.
- [25] P. Palies, D. Durox, T. Schuller, S. Candel, Experimental study on the effect of swirler geometry and swirl number on flame describing functions, *Combust. Sci. Technol.* 183 (2011) 704–717, <https://doi.org/10.1080/00102202.2010.538103>.
- [26] C.F. Silva, F. Nicoud, T. Schuller, D. Durox, S. Candel, Combining a Helmholtz solver with the flame describing function to assess combustion instability in a premixed swirled combustor, *Combust. Flame* 160 (2013) 1743–1754, <https://doi.org/10.1016/j.combustflame.2013.03.020>.
- [27] J.F. Bourguoin, D. Durox, J.P. Moeck, T. Schuller, S. Candel, A new pattern of instability observed in an annular combustor: The slanted mode, *Proc. Combust. Inst.* 35 (2015) 3237–3244, <https://doi.org/10.1016/j.proci.2014.06.029>.
- [28] D. Laera, T. Schuller, K. Prieur, D. Durox, S.M. Camporeale, S. Candel, Flame describing function analysis of spinning and standing modes in an annular combustor and comparison with experiments, *Combust. Flame* 184 (2017) 136–152, <https://doi.org/10.1016/j.combustflame.2017.05.021>.
- [29] D. Iurashev, G. Campa, V.V. Anisimov, E. Cosatto, L. Rofi, Application of a three-step approach for prediction of combustion instabilities in industrial gas turbine burners, in: *Proceedings of the 1st Global Power and Propulsion Forum, Zurich, Switzerland, 16-18 January 2017*, 2017 paper no GPPF-2017-24.
- [30] S. Tufano, P. Stopford, J.C. Roman Casado, J.B.W. Kok, Modelling flame-generated noise in a partially premixed, bluff body stabilised model combustor, in: *Proceedings of the ASME Turbo Expo 2012, Copenhagen, Denmark, 11-15 June 2012*, 2012, <https://doi.org/10.1115/GT2012-69501> paper 2012-69501.
- [31] L. Tay-Wo-Chong, W. Polifke, Large eddy simulation-based study of the influence of thermal boundary condition and combustor confinement on premix flame transfer functions, *J. Eng. Gas Turbines Power* 134 (2013), <https://doi.org/10.1115/1.4007734> paper no 021502.

- [32] J.S. Hardi, M. Oschwald, Cryogenic oxygen jet response to transverse acoustic excitation with the first transverse and the first combined longitudinal-transverse modes, *Progress in Propulsion Physics* 8 (2016) 75–94, <https://doi.org/10.1051/eucass/201608075>.
- [33] C.V. da Silva, H.A. Vielmo, F.H.R. França, Numerical simulation of the combustion of methane and air in a cylindrical chamber, *Engenharia Térmica (Thermal Engineering)* 5 (2006) 13–21.
- [34] M. Bauerheim, F. Nicoud, T. Poinsot, Progress in analytical methods to predict and control azimuthal combustion instability modes in annular chambers, *Phys. Fluids* 28 (2016), <https://doi.org/10.1063/1.4940039>. Article Number: 021303.
- [35] F. Eisinger, R. Sullivan, Evaluation of non-vibrating utility burner/furnace systems for resistance to thermoacoustic oscillations, in: *Proceedings of the ASME Pressure Vessels and Piping Conference*, 23-27 July 2006, Vancouver, Canada, 2006. Paper PVP 2006-ICPVT-11-93054.
- [36] F. Eisinger, R. Sullivan, Prediction of thermoacoustic vibration of burner/furnace systems in utility boilers, *J. Press. Vessel Technol.* 130 (2008), 015002, <https://doi.org/10.1115/1.2826459>.
- [37] M.A. Heckl, M.S. Howe, Stability analysis of the Rijke tube with a Green's function approach, *J. Sound Vib.* 305 (2007) 672–688, <https://doi.org/10.1016/j.jsv.2007.04.027>.
- [38] M.A. Heckl, M.S. Howe, The Rijke tube: Green's function approach in the time and frequency domain, in: *Proceedings of the 14th International Congress on Sound and Vibration*, Cairns, Australia, 9-12 July 2007, 2007.
- [39] P.M. Morse, U. Ingard, *Theoretical Acoustics*, Princeton University Press, Princeton, 1986.
- [40] X. Sun, X. Wang, L. Du, X. Jing, A new model for the prediction of turbofan noise with the effect of locally and non-locally reacting liners, *J. Sound Vib.* 316 (2008) 50–68, <https://doi.org/10.1016/J.JSV.2008.02.053>.
- [41] W.H. Press, B.P. Flannery, S.A. Teukolsky, W.T. Vetterling, *Numerical Recipes*, Cambridge University Press, Cambridge, 1986.
- [42] Candel, S., Huynh, C. & Poinsot, T. (2012) Some Modelling Methods of Combustion Instability. Chapter 5 in: *Unsteady Combustion* (ed. Culick, F., Heitor, M.V. & Whitelaw J.H.). Kluwer Academic Publishers, Dordrecht.
- [43] L.E. Kinsler, A.R. Frey, A.B. Coppens, J.V. Sanders, *Fundamentals of Acoustics*, 3rd edition, John Wiley and Sons, New York, 1982.
- [44] C.A. Coulson, A. Jeffrey, *Waves*, 2nd edition, Longman, London, 1977.
- [45] W. Na, G. Efraimsson, S. Boij, Numerical prediction of thermoacoustic instabilities with a V-flame, in: *Proceedings of the 23rd International Congress on Sound and Vibration*, Athens, Greece, 10-14 July 2016, 2016.
- [46] S.M. Gopinathan, D. Iurashev, A. Bigongiari, M. Heckl, Nonlinear analytical flame models with amplitude-dependent time-lag distributions, *Int. J. Spray Combust. Dyn.* 10 (2018) 264–276, <https://doi.org/10.1177/1756827717728056>.
- [47] S.M. Gopinathan, A. Bigongiari, M. Heckl, Analytical approximations for heat release rate laws in the time- and frequency-domains, *Int. J. Spray Combust. Dyn.* 12 (2020) 1–14, <https://doi.org/10.1177/1756827720930491>.